HHS Public Access

Author manuscript

Nat Cell Biol. Author manuscript; available in PMC 2024 October 01.

Published in final edited form as:

Nat Cell Biol. 2024 April ; 26(4): 581–592. doi:10.1038/s41556-024-01382-2.

Disordered C-terminal domain drives spatiotemporal confinement of RNAPII to enhance search for chromatin targets

Yick Hin Ling[1], **Ziyang Ye**[1,*], **Chloe Liang**[1,*], **Chuofan Yu**[1,*], **Giho Park**[1,*], **Jeffry L. Corden**[2], **Carl Wu**[1,2]

[1]Department of Biology, Johns Hopkins University, Baltimore, USA

[2]Department of Molecular Biology and Genetics, Johns Hopkins University School of Medicine, Baltimore, USA

Abstract

Efficient gene expression requires RNA Polymerase II (RNAPII) to find chromatin targets precisely in space and time. How RNAPII manages this complex diffusive search in 3D nuclear space remains largely unknown. The disordered carboxy-terminal domain (CTD) of RNAPII, which is essential for recruiting transcription-associated proteins, forms phase-separated droplets *in vitro*, hinting at a potential role in modulating RNAPII dynamics. Here, we use single-molecule tracking and spatiotemporal mapping in living yeast to show that the CTD is required for confining RNAPII diffusion within a subnuclear region enriched for active genes, but without apparent phase separation into condensates. Both Mediator and global chromatin organization are required for sustaining RNAPII confinement. Remarkably, truncating the CTD disrupts RNAPII spatial confinement, prolongs target search, diminishes chromatin binding, impairs pre-initiation complex formation, and reduces transcription bursting. This study illuminates the pivotal role of the CTD in driving spatiotemporal confinement of RNAPII for efficient gene expression.

Introduction

The carboxy-terminal domain (CTD) of RPB1 (Rpo21 in yeast), the largest subunit of RNA Polymerase II (RNAPII), is an essential and unique structural feature crucial for transcription regulation in eukaryotes. Defined by its intrinsically disordered structure[1] and consensus heptad repeats (YSPTSPS)[2], the CTD acts as a docking platform for recruiting transcription-associated proteins to interact with RNAPII[3–5]. Mutations or truncations of CTD repeats affect cell viability[6–10] and impair gene activation[11–17]. Notably, the number of the heptad repeats in the CTD correlates with genome size throughout eukaryotes[13,18,19].

Corresponding author: Carl Wu; wuc@jh.edu.

*Equal contribution

Author Contributions Statement

Y.H.L., J.L.C., and C.W. designed the experiments. Y.H.L. performed the experiments and analyzed the data. Z.Y. performed SMT on Hsf1-Halo in the wildtype background. G.P. contributed to the initial trial of spatiotemporal mapping. Z.Y., C.L., and C.Y. assisted in experiments. Y.H.L., J.L.C., and C.W. wrote the manuscript. Z.Y., C.L., C.Y. and G.P. contributed equally.

Competing Interests Statement

The authors declare no competing interests.

Code availability

Custom code can be found at GitHub (https://github.com/yhinling/Ling-et-al-2024).

The biochemical and biophysical properties of intrinsically disordered regions (IDRs), including the CTD, allow liquid-liquid phase separation (LLPS) through weak-multivalent transient interactions[20–22]. This results in the formation of phase-separated transcription condensates comprising RNAPII, the Mediator complex and other transcription-related proteins. These condensates have been proposed to play a critical role in organizing the transcription machinery to facilitate gene regulation[20–25]. By creating a specialized subnuclear environment, LLPS may help increase the concentration of RNAPII and associated factors for efficient transcription[26,27]. *In vitro*, the size of the phase-separated droplets formed by the biochemically purified CTD is dependent on its length. For example, the human RNAPII CTD, which has 52 heptad repeats, twice as many as its yeast counterpart with 26 repeats, readily forms larger droplets[20,22]. However, there is considerable debate concerning the relationship between *in vitro* reconstituted LLPS and its role as the primary mechanism in the formation of specific membraneless compartments within the cell[28–31]. Specifically, whether phase-separated RNAPII condensates represent a universally conserved mechanism, or if weak interactions driven by disordered CTDs can guide RNAPII diffusion without transitioning into a condensed phase in the living cell remains unclear. Here, we combined live-cell, single-molecule tracking with yeast genetics to elucidate the intricate diffusive mechanisms of RNAPII and the causal dependencies of its target search. Our results show that the freely diffusing RNAPII is spatially confined, but does not instigate formation of phase-separated condensates on a microscopic scale. The spatial confinement of RNAPII is governed by the full-length CTD, and requires both Mediator and global yeast chromatin organization. Importantly, such confinement allows freely diffusing RNAPII to stochastically oversample subnuclear regions enriched with active genes, establishing a highly efficient target search mechanism to enhance pre-initiation complex (PIC) formation and transcription bursting. Our work demonstrates how RNAPII leverages its search strategy as a rate-limiting step to promote transcription activation, providing insights on the functional significance of the CTD in regulating the spatiotemporal dynamics of RNAPII.

Results

Spatiotemporal mapping of transcription machinery

We performed live-cell single-molecule tracking (SMT) of fluorescently labeled endogenous RNAPII and other transcription proteins fused to HaloTag, and expressed as sole source under native promoter control (Fig. 1b, Extended Data Fig. 1e). Molecule trajectories were categorized into chromatin-bound or freely diffusing states based on diffusivity, geometry and angular orientation using a multi-parameter classification approach (Fig. 1a, Extended Data Fig. 1d and 2). To extract the spatiotemporal dynamics of the transcription machinery in the small budding yeast nucleus, we developed a mapping method for a strain with GFP markers delineating the plasma membrane, nuclear envelope and the nucleolus (Extended Data Fig. 1a–c and Supplementary Video 1). The method involves selection of G1 phase cells exhibiting minimal nuclear drift with distinct nuclear envelope and nucleolar boundaries (Extended Data Fig. 1g and 3a), superposition of single-molecule localizations from multiple (>10) cell nuclei projected on a 2D plane. The captured single-molecule localizations do not contain any z-information, and the axes of the projected

plane correspond to x and y coordinates (Fig. 1a). This maps the spatial distribution of chromatin-bound and freely diffusing proteins over an integrated timeframe, and is grounded in the physical constraints imposed on the centromeres and telomeres of yeast interphase chromatin[32–35] (Extended Data Fig. 1b). A similar mapping approach was previously described for the spatial probability density of single gene loci in yeast[36]. Likewise, we interpret the presented spatiotemporal map density as the probability density of protein localization over time, rather than instantaneous protein clustering.

We validated the method by mapping the trajectories of free HaloTag, chromatin-bound centromeric Cse4 and telomeric Sir4 to the expected centromere (Cse4) and nuclear periphery regions (Sir4) established in the literature[32–35] (Extended Data Fig. 3f,g). We next examined essential transcription proteins RNAPII, RNAPI, RNAPIII, TFIID, and SAGA, showing their free and bound diffusion coefficient distributions and corresponding fractions (Fig. 1b), and the spatiotemporal distribution of bound populations (Fig. 1c). As a reference for the distribution of bound transcription proteins, we generated a 2D projection of a 3D yeast genome model derived from 3C experimental data[37] (Extended Data Fig. 3d). Integrating sequence coordinates (obtained from Saccharomyces Genome Database) of highly expressed genes across multiple gene classes[38] allowed us to highlight their probability density distributions on the genome simulation map. Other investigations have similarly utilized 3D yeast genome models derived from polymer chain simulation to determine the probability densities of specific gene classes, such as tRNA genes and highly expressed mRNA genes[39,40]. Unlike the semi-homogenous H2B density map (Fig. 1c; bottom), the bound transcription protein maps (Fig. 1c) are uniquely distinct, and spatially show resemblance to the corresponding functional gene classes located by genome simulation[37] (Fig. 1d). Notably, chromatin-bound TFIID and SAGA exhibit distinct spatial territories in the spatiotemporal maps (Fig. 1c), mirroring the TATA-less (TFIID-dominated) and TATA-containing (SAGA-dominated) genes[41] respectively in the genome simulations (Fig. 1d), raising the possibility that the regulation of gene classes may be related to their spatial positioning[39,40]. Further investigation is needed to fully understand the implications of this organization.

CTD governs chromatin binding and confinement of free RNAPII

Given structural similarities between the three eukaryotic RNA polymerases, we compared the spatiotemporal distribution and diffusivity of RNAPII with RNAPI and RNAPIII. Freely diffusing RNAPII shows a higher degree of nucleolar exclusion (Extended Data Fig. 4a–c), and diffuses more slowly than expected from its molecular weight (Extended Data Fig. 4d). We hypothesized that the distinct spatiotemporal dynamics of freely diffusing RNAPII might be partially attributed to its large hydrodynamic radius due to the presence of the disordered CTD on its largest subunit, RPB1[Rpo21] [42,43], a feature absent from RNAPI and RNAPIII (Fig. 2a and Extended Data Fig. 4e,f). Notably, we observed that increasing the number of CTD heptad repeats across a spectrum of 0, 8, 9, 10, 15, 20, 26 (wildtype), 52, 78, to 104 repeats led to increased nucleolar exclusion and decreased diffusion coefficient of free RNAPII (D_{free}) (Fig. 2b and Extended Data Fig. 4g). This indicates that CTD length might directly and/or indirectly modulate the diffusivity and distribution of RNAPII between nucleolus and nucleoplasm. A large hydrodynamic radius, conferred by a long and

highly disordered CTD, would slow RNAPII and limit diffusion into the nucleolus via size exclusion, thereby increasing its effective concentration in the nucleoplasm. As noted below, there are additional mechanisms relevant to RNAPII nucleoplasmic distribution.

Next, we explored the impact of CTD length on the chromatin-bound population of RNAPII. Progressive truncation of the CTD from 26 repeats to 20, 15, 10, 9, 8, and 0 repeats notably reduces its bound fraction, whose low diffusion coefficient is comparable to bound H2B (D_{bound} ~0.05 μm^2/s) (Fig. 1b, 2d, Extended Data Fig. 5a and Supplementary Video 2). Conversely, extending the CTD to 52, 78, and 104 repeats shows a trend toward an increase in this fraction, suggesting potential enhancement of chromatin association (Fig. 2c and Extended Data Fig. 5a). This trend remains consistent after normalization of nuclear RPB1^{Rpo21} fluorescence to the expression level across mutants[13] (Extended Data Fig. 5c,d). We primarily focus on CTD truncations due to their pronounced effects; The spatiotemporal maps show a global reduction of RNAPII binding for truncated CTD strains CTD9 and CTD0 (Fig. 2e; top). Importantly, the map of free RNAPII shows spatial confinement in a subnuclear region enriched for the bound population (Fig. 2e), an area also abundant in highly expressed yeast genes (Fig. 1d and Extended Data Fig. 3e). This confinement is disrupted in the CTD9 mutant, and further reduced in CTD0 (Fig. 2e; bottom). Hence, the CTD has a critical role in the spatiotemporal dynamics for both bound and free RNAPII.

RNAPII confinement characterized by anisotropic diffusion

We quantified the spatiotemporal confinement of freely diffusing RNAPII by measuring anisotropy, using the ratio of extreme backward to forward angles ($f_{180/0}$) of free trajectories in the nucleoplasm, with confined trajectories showing backward bias[44] (Fig. 3a,b; top and Supplementary Video 3). We observed a substantial backward bias in wildtype (WT) RNAPII-CTD26, which is largely absent for RNAPII-CTD9 and RNAPII-CTD0 mutants, and free HaloTag (Fig. 3a,b). On the other hand, CTDs expanded to 52, 78, and 104 repeats show increasing anisotropy (Extended Data Fig. 6c). A $f_{180/0}$ peak around 150 nm (Fig. 3b) suggests RNAPII confinement within potential domains, as reported for CTCF in mammalian cells, in which ‘anisotropic diffusion through transient trapping in zones’ has been proposed as an explanatory model[44]. Given that yeast interphase chromosomes are physically tethered to the nuclear envelope via telomeres, we disrupted global chromatin organization by inducing telomere detachment through deletion of *esc1* and *yku70*[45] (Fig. 3c,d and Supplementary Video 4). This resulted in a slight reduction of RNAPII binding (Fig. 3e). Notably, telomere detachment abolishes the $f_{180/0}$ peak at 150 nm, but maintains elevated $f_{180/0}$ across length scales as compared to that of CTD truncation mutants (Fig. 3f,g). This suggests that global chromatin organization might be required for establishing transient trapping zones or domains[46] that contribute to RNAPII confinement kinetics.

Given the reported weak interactions between mammalian Mediator IDRs and RNAPII CTD *in vitro*[22], we investigated the role of Mediator in the diffusion confinement of free RNAPII. We observed a significant reduction of RNAPII binding when Mediator is degraded using an auxin-inducible degron strain (MED14^{Rgr1} AID) (Fig. 3h,i). Importantly, there is a large reduction of backward bias as shown in the angle distribution plots and anisotropy ($f_{180/0}$) for free RNAPII (Fig. 3j,k). Furthermore, spatiotemporal mapping indicates a considerable

decrease in free RNAPII confinement (and in the nucleoplasm/nucleolus ratio) following Mediator degradation (Extended Data Fig. 7b,d). For RNAPII-CTD9, Mediator degradation similarly decreased its confinement and further reduced the bound fraction (Extended Data Fig. 7j,k). Additionally, there is partial overlap between the probability density maps of bound Mediator and the confined trajectories of free RNAPII-CTD26 (Extended Data Fig. 7a). Collectively, we conclude that Mediator is required for RNAPII diffusion confinement in the nucleoplasmic compartment.

No substantial RNAPII clustering observed

The confined diffusion of RNAPII raises the question of phase separation in condensates. We did not observe fluorescent RNAPII puncta under wide-field microscopy in RPB1^{Rpo21}-HaloTag fusions harboring WT or CTD mutants with reduced or expanded repeats (Fig. 4a). To investigate the possibility of nanoscale puncta, we performed fixed-cell stochastic optical reconstruction microscopy (STORM) on RPB1^{Rpo21}-HaloTag co-stained with JF552 and JFX650. We imaged two color channels simultaneously and performed pairwise cross-correlation C(r) analysis to account for clustering artifacts due to fluorophore blinking[47] (Fig. 4b). The C(r) values for RNAPII-CTD26, similar to those of H2B and RNAPII-CTD9, are close to 1, suggesting no significant clustering (Fig. 4c). A recent *in vitro* study suggests that multiple yeast RNAPII molecules could bind to a single UAS (upstream activating sequence)[48]. While our low C(r) values do not exclude the presence of minute or infrequent clustering, the bulk of RNAPII exhibits a dispersed distribution.

Given the possibility that transient clusters could be missed by imaging of fixed cells, we replicated the co-staining experiment using live yeast. We analyzed the data using multiple short time windows for potential time-correlated detections[24], and performed Monte Carlo simulations to account for high C(r) values resulting from the limited number of detections within brief observation windows. Nonetheless, we found no strong statistical evidence for transient RNAPII clustering (Fig. 4d; top). Notably, pairwise correlation g(r) analysis performed using only JF552 indicated strong clustering due to repetitive fluorophore blinking or overcounting of fluorophores with extended lifetimes (Fig. 4d; bottom), which underscores the importance of two-color staining for reliable cluster assessment[47]. Thus, the observed high probability density of free RNAPII over time in our spatiotemporal map (Fig. 2e; bottom) results from transient confinement, rather than stable clustering or phase separation into condensates. This implies that despite the spatial confinement of RNAPII in subnuclear regions, its overall distribution at any given time remains broadly homogeneous. Consistent with this, Mediator degradation, which reduces RNAPII chromatin binding (Fig. 3i) and anisotropy ($f_{180/0}$) (Fig. 3k), shows no substantial change in the diffusion coefficient of free RNAPII (Extended Data Fig. 7c). This suggests that the free RNAPII confinement is transient, and that the overall mobility over time, which is reflected in the diffusion coefficient, remains largely unchanged.

CTD length is critical for RNAPII target search kinetics

To further investigate the role of the CTD in controlling the chromatin binding kinetics of RNAPII, we measured the residence time of individual RNAPII binding events using the ‘slow-tracking’ SMT mode that minimizes photobleaching with low laser power (Fig.

5b, Extended Data Fig. 8c,d and Supplementary Video 5). Halo-H2B cells were imaged as a spike-in control to correct for photobleaching and chromatin movements out of the focal plane (Fig. 5a and Extended Data Fig. 8f). We observed an average stable residence time of ~20 s for WT RNAPII-CTD26, which encompasses nonproductive and productive pre-initiation, initiation, elongation, and termination. For RNAPII-CTD9, this average value is reduced substantially to ~10 s, and the stably bound fraction decreases from ~16% to ~3% (Fig. 5c–e). Structural investigations have shown that CTD repeats make specific contacts with the Mediator complex[49]. The short residence time of RNAPII-CTD9 is therefore likely due to compromised pre-initiation complex (PIC) recruitment and engagement with the Mediator[50] (Fig. 5j). Similarly, when Mediator is degraded, the WT RNAPII-CTD26 stably bound fraction is decreased, and the residence time even further reduced to ~5 s (Fig. 5g–i), consistent with previous ChIP results showing depletion of RNAPII occupancy across nearly all genes under similar degron conditions[51]. Consistent with this, Mediator degradation also leads to an additional decrease in the stably bound fraction of RNAPII-CTD9, with residence time further reduced from ~10 s to ~4 s (Extended Data Fig. 7l–n).

We estimated the target search time of RNAPII, i.e. the average search duration for an RNAPII molecule between two stable binding events including intervening 3D diffusion and multiple transient chromatin associations, to be ~120 s (Fig. 5f). Although there is no significant change in target search time for the telomere attachment mutant *esc1Δ yku70Δ*, we found that the CTD9 mutant indeed shows prolonged RNAPII target search, increasing from the WT value of ~120 s to ~350 s (Fig. 5f). This observation is consistent with the marked reduction in spatiotemporal confinement of CTD9 and CTD0 mutants (Fig. 2e; bottom and 3b), suggesting that this confinement facilitates the RNAPII search for and association with promoter chromatin.

CTD controls PIC chromatin-binding and transcription bursts

In addition to facilitating RNAPII search for chromatin targets, CTD is a versatile scaffold coordinating the recruitment and release of transcription initiation, elongation and termination factors throughout the transcription cycle[3,4]. Accordingly, we examined the effects of CTD truncation on the dynamics of PIC components. In the CTD9 mutant, the bound fractions of TFIIA (Halo-Toa1), TFIIB (Sua7-Halo), TFIIE (Tfa1-Halo), TFIIF (Tfg1-Halo), and TFIIH (Tfb4-Halo and Kin28-Halo), but not TBP (Halo-Spt15), TFIID (Taf1-Halo), SAGA (Spt7-Halo and Spt8-Halo) and Mediator (Rgr1-Halo and Med1-Halo), are substantially decreased (Fig. 6a,b). This reduction is consistent with the crucial role of the CTD in maintaining the integrity of the PIC by facilitating key interactions[49,50,52]. The modest binding changes for two core subunits of Mediator (Rgr1 and Med1) suggest that other interactions besides CTD binding contribute to its stability on chromatin.

We next examined the transcriptional regulation of heat shock response genes in the CTD9 mutant, due to its temperature-sensitive phenotype[7]. Hsf1, the master transcriptional regulator of the heat shock response genes[53], constitutively associates with heat shock elements (HSEs) at the promoter[54–57] under both non-heat shock (NHS) and heat shock (HS) conditions (Fig. 7f). The spatiotemporal map reveals a high density of bound Hsf1 near the nuclear envelope, similar to highly expressed Hsf1 gene targets in the genome

simulation map (Fig. 7a,b). Likewise, the position of the highly expressed Hsf1 target gene *HSP104* exhibits a similar peripheral localization as determined by computational polymer modeling[58]. Hsf1 is highly dynamic, with over ~85% of molecules that are freely diffusing (Fig. 7c and Extended Data Fig. 9a). Heat shock induction increases Hsf1 binding from ~10% to ~20% (stable binding from ~2% to ~5%) during the acute response (0–20 min at 39°C) (Fig. 7c,d), maintaining a ~5 s residence time for NHS and acute HS conditions (Fig. 7e and Extended Data Fig. 9b). Prolonged HS (20–40 min at 39°C) slightly reduces Hsf1 binding fraction to ~15% (~3% stable binding) (Fig. 7c,d and Extended Data Fig. 9a), with a decrease of residence time to ~2.5 s (Fig. 7e and Extended Data Fig. 9b). In the CTD9 mutant, Hsf1 binding and residence time during the acute heat shock response remains largely unchanged compared to the WT (Fig. 7c–e and Extended Data Fig. 9a,b), suggesting that CTD truncation has a minimal impact on the observed binding dynamics of the upstream transcription factor Hsf1.

To address the functional consequences of CTD truncation, we focused on *HSP82*, which is expressed constitutively under Hsf1 control and is highly inducible on heat shock. Previous research has emphasized the importance of CTD length in transcription activation[11–17] and in the transcription bursting of *GAL* genes[13], which are expressed only under inducible conditions. It is unclear whether the CTD controls the burst kinetics of constitutively expressed genes. We examined transcription bursting of *HSP82* by imaging the binding of fluorescently-tagged PP7 coat protein (PP7CPx2-mScarlet-Ix3) to a 24xPP7 sequence inserted into the 5’ UTR of the nascent *HSP82* mRNA (Fig. 7f,g and Supplementary Video 6). Strong fluorescent foci of PP7CPx2-mScarlet-Ix3 representing *HSP82* transcription sites (TSs), frequently appear near the nuclear envelope (Fig. 7h–j), consistent with the spatiotemporal map of bound Hsf1 (Fig. 7a,b). Under nonshock conditions, CTD9 shows a lower percentage of cells with *HSP82* TS fluorescence (~78%) compared to WT (~96%). However, upon heat shock, TS fluorescence appears almost instantaneously in nearly all cells for both WT and CTD9 mutant strains (Fig. 7k,l). We calculated the corresponding transcription ON and OFF times after binary conversion of *HSP82* TS signals (Fig. 7k). For WT CTD26, acute heat shock increases the *HSP82* ON time from ~3 min to ~4.5 min, while decreasing the OFF time from ~7 min to ~2 min. For prolonged heat shock, the ON time is similar to nonshock conditions, while the OFF time is reduced to ~3 min (Fig. 7m,n, and Extended Data Fig. 9c,d), anticipating attenuation of the heat shock response. Notably, in all conditions, the CTD9 mutant consistently reduces the ON time (lower burst duration) and increases the OFF time (lower burst frequency) of *HSP82* transcription (Fig. 7m,n and Extended Data Fig. 9c,d), indicating that full CTD length is required for optimal burst kinetics under both constitutive and heat shock conditions. This finding offers a molecular explanation for the temperature-sensitive phenotype in the CTD9 mutant[7]. Importantly, the reduction in both duration and frequency of transcription bursting indicates that the diffusion confinement of RNAPII in the nucleoplasm could regulate the rate-limiting search for chromatin targets in the transcription cycle to sustain a transcription burst. The number of intrinsically disordered CTD repeats is central to this spatiotemporal confinement.

Discussion

We have extended single-molecule tracking (SMT) to develop global spatiotemporal maps of transcription protein dynamics in living yeast (Fig. 1). This approach reveals that the disordered CTD of RNAPII, with a WT length of 26 heptad repeats, directs the confinement of RNAPII within a subnuclear region enriched for active genes (Fig. 2). Characterization of anisotropic diffusion of RNAPII shows its dependence on the full-length CTD, and on chromatin organization and the presence of Mediator (Fig. 3). RNAPII exhibits transient confinement without phase separation into condensates (Fig. 4). Importantly, the number of CTD repeats critically influences RNAPII search kinetics (Fig. 5) and PIC formation (Fig. 6). Furthermore, CTD truncation functionally disrupts transcription burst kinetics of *HSP82* (Fig. 7).

Our observations in yeast demonstrate that RNAPII does not exhibit substantial clustering, questioning the generality and the extent of LLPS involvement in its spatial organization. For eukaryotes with larger nuclei and genome complexity, additional spatial control and dynamic phase-separated compartments might be necessary for long range promoter-enhancer interaction[59,60], although this is a topic of ongoing study. In yeast, however, the strong physical constraints and subnuclear chromosome tethering[32–35], alongside the compact genome, could create domains enriched for active genes (Fig. 1c,d), and facilitate RNAPII transient confinement without the need for phase separation into condensates (Fig. 3 and 4). Furthermore, the concentration of RNAPII in yeast (1,200 molecules per μm^3, assuming a nuclear radius of 1 μm, and 5,000 RNAPII per nucleus (least abundance subunit Rpb9; SGD)) is ~30-fold higher than in human U2OS cell nuclei (~40 molecule per μm^3)[61]. Such a high endogenous RNAPII concentration in yeast suggests that transient confinement might be sufficient for efficient target search. Furthermore, the yeast nucleoplasmic environment may be less favorable for phase separation into condensates compared to higher eukaryotes.

What might be the molecular basis of the spatiotemporal confinement of yeast RNAPII? Weak interactions observed *in vitro* between the IDRs of the RNAPII CTD and those of the Mediator complex[20–22] (Supplementary Fig. 3), hint at a potential mechanism involving IDR interactions that remains to be further elucidated. Imaging of the CTD fused to GFP shows evidence of enrichment at transcriptionally active loci of *Drosophila* polytene chromosomes *in vivo*[62], raising the question whether the CTD alone is sufficient to drive its own spatiotemporal confinement in living yeast. Our supplementary observations show that HaloTag alone and Halo-CTD fusions harboring 26, 52, 78, and 104 heptad repeats expressed under control of the native *RPO21* promoter exhibit minimal chromatin binding (Extended Data Fig. 10a), show no puncta formation (Extended Data Fig. 10b), and D_{free} values aligning with the Stokes-Einstein equation, indicating uniform nucleoplasmic viscosity (~30 cP) without phase separation (Extended Data Fig. 10d–g). Furthermore, Halo-CTD mutants do not exhibit high $f_{180/0}$ values, indicating that diffusion is relatively isotropic or unconfined in the yeast nucleus (Extended Data Fig. 10h). Evidently, at physiological expression levels, the CTD alone does not induce the same degree of diffusion confinement as observed for the RNAPII complex. Thus, the CTD is necessary, but not sufficient for

the spatiotemporal confinement of RNAPII, and additional factors or domains within the RNAPII complex might come into play.

Our data suggest that transient diffusion confinement of RNAPII dependent on CTD repeats and the Mediator facilitates the rate-limiting search for chromatin targets early in the transcription cycle (Fig. 7o). In particular, transient confinement of diffusing RNAPII could increase the probabilities of intermolecular interactions and specific association rates with the Mediator and other PIC components, promoting repeated rounds of transcription to generate a transcription burst. Our study emphasizes the crucial role of the CTD in driving RNAPII target search and shaping the spatiotemporal dynamics of PIC assembly, highlighting its multifaceted functions in the pathway to gene expression.

Methods

Yeast strain construction

All *Saccharomyces cerevisiae* strains in this study (Supplementary Table 2) are isogenic derivatives of BY4741 with *pdr5Δ* deletion for enhanced HaloTag ligand labeling. Yeast strains were generated using standard yeast transformation. Free HaloTag was fused with a bipartite nuclear localization signal (NLSx2; KRTADGSEFESPKKKRKV) at the N-terminus for nuclear localization. Strains with *pdr5Δ* and GFP markers exhibit growth identical to the WT (Extended Data Fig. 5i). Strains with defects in promoter scanning and transcription start site (TSS) selection by the PIC exhibit sensitivity to mycophenolic acid (MPA). This sensitivity is reflected in the inability of the PIC to shift to the downstream *IMD2* TSS in the presence of MPA, as observed in certain mutations of TFIIF and TFIIH[71]. Growth of strains with HaloTag fusions to various PIC component subunits was tested on SC-MPA (20 μg/ml) agar plates, and those showing no MPA sensitivity phenotype were selected for further analysis (Extended Data Fig. 5k). The procedure for inserting 24xPP7 into the 5' UTR of *HSP82* was performed as previously described[72]. All RPB1^{Rpo21} CTD length mutants preserve the tip domain. For CTD0 experiments, RPB1^{Rpo21}-CTD0-Halo, under native promoter control, was integrated ectopically in RPB1^{Rpo21}-CTD26 (WT) AID background (Extended Data Fig. 5e,f,j). This setup ensures cell viability as CTD0 alone is lethal. During imaging, the WT RNAPII-CTD26 was degraded by auxin treatment, thus permitting the investigation of RNAPII-CTD0 dynamics without interference from the WT copy.

For generation of the CTD mutants, HaloTag fusions and CTD manipulation of *RPO21* involve integrating the *URA3* gene downstream of *RPO21* (*RPO21-URA3*) and replacing *RPO21-URA3* with *RPO21*-CTD-Halo constructs via counter-selection in 5-fluoroorotic acid (5-FOA). All CTD mutants retain the tip domain, and non-consensus heptads are preserved in CTD truncation mutants (Fig. 2a and Supplementary Table 1). For CTD expansion mutants, multiple consensus heptad 'YSPTSPS' are inserted between heptads 15 and 16. To facilitate CTD modification, we engineered a CTD26-encoding DNA sequence with silent mutations to create restriction enzyme sites, referred to as nCTD26 (Supplementary Table 1). Yeast strains with nCTD26 exhibit growth rates identical to WT (Extended Data Fig. 5i).

Microscope setup

All imaging was performed using a custom-built Axio Observer Z1 microscope (Zeiss, Germany) equipped with a 150X glycerin immersion objective (ZEISS, Germany) (Supplementary Fig. 1). Data were collected with an EM-CCD camera (C9100-13, Hamamatsu Photonics, Japan) featuring 16 μm physical pixel size and 107 nm pixel size in recorded images. The camera was controlled by HCImage 5.0.1. The laser excitation wavelengths used were 555 nm for JF552 and mScarlet-Ix3, 637 nm for JFX650 and miRFP670nano3, and 488 nm for GFP. For simultaneous two-color STORM imaging, emission lights were split by W-VIEW GEMINI (A12801-01, Hamamatsu Photonics, Japan). Detailed information on emission and excitation filters is described previously[73].

Single-molecule tracking (SMT)

Yeast cultures grown in Synthetic Complete medium (SC) were treated with JF552-HaloTag ligand at the early log phase (OD_{600} = 0.2–0.3) for 4 hours. HaloTag fusions were sparsely labeled with dye concentrations adjusted for factor abundance. Cells were washed at least six times, adhered to concanavalin A-treated coverslips in cell chambers (Invitrogen, Cat. No. A7816) and imaged at room temperature. Initial exposure to a 555 nm laser yielded a bright nuclear signal, followed by transient shelving of fluorophores in a metastable dark state. JF552 spontaneously and stochastically reverted to a fluorescent state, resulting in sparse single-molecule localization[74,75] (Extended Data Fig. 1e). Fast tracking (10 ms/frame) was performed with continuous 555 nm laser irradiation at ~1 kW/cm^2 to extract bound and free molecule dynamics (Supplementary Video 2). Static localization error was 18.9 ± 7.7 nm for Halo-H2B in fixed cells, and 22.0 ± 9.0 nm in live cells. Slow tracking (250 ms/frame) was performed with continuous 555 nm laser irradiation at a lower laser power of ~0.035 kW/cm^2 to minimize photobleaching and enhance residence time measurement resolution (Supplementary Video 5). We routinely measured and adjusted laser power and alignment throughout imaging sessions to account for minor fluctuations. Imaging sessions lasted two hours, equivalent to one cell cycle in SC at room temperature; Cse4-$Halo^{Internal}$ was imaged for only one hour due to its short centromeric half-life. Laser exposure during imaging did not appear to induce any significant changes in cell cycle progression (Extended Data Fig. 1f).

Localizing and tracking single molecules

Single-molecule localization and trajectory linking were conducted using Diatrack software[76]. For fast tracking, a 6-pixel (642 nm) max jump was applied, and a 3-pixel (321 nm) max jump for slow tracking. Only G1 phase cells were analyzed, with nuclear masks manually drawn based on GFP nuclear landmarks to exclude trajectories outside the nucleus (Extended Data Fig. 3a). Single-step disappearances of bound molecules were observed in both fast and slow tracking, indicating accurate identification of single molecule signals (Extended Data Fig. 8a–d)

Fast-tracking data analysis

Selection of Nuclei—A typical imaging session comprises around 40 movies, each containing approximately 3 in-focus cell nuclei. Given the dynamic nature of yeast nuclei,

we carefully selected G1 cells exhibiting minimal nuclear drift during imaging (Extended Data Fig. 1g and 3a). This stringent selection process typically resulted in an average of only 5 suitable nuclei per session being chosen for further analysis. For sufficient localization data, all datasets included a minimum of 10 cell nuclei and 1000 trajectories, obtained from at least two independent imaging sessions.

Brief overview of multi-parameter classification—We used vbSPT[77] (adapted script from Hansen et al.[44]) to perform two-state hidden Markov model (HMM) analysis to differentiate transitioning trajectories and separate single-state segments into individual trajectories. We acknowledge the possibility of classifying trajectories into more than two diffusive states. However, Brownian simulations suggest that subdividing a freely diffusing trajectory into multiple states could create artifacts, particularly when the experimental data is dominated by short trajectories (Supplementary Fig. 2a). Short trajectories might lack sufficient information for accurate sub-classification, and any apparent confinement or directionality could stem from partial observation of the inherent randomness (Supplementary Fig. 2).

Following the HMM analysis, we calculated 10 parameters that describe the diffusivity, geometry and angular orientation of each trajectory (Fig. 1a, Extended Data Fig. 2g). We then applied Uniform Manifold Approximation and Projection (UMAP) for dimensionality reduction, which was semi-supervised by the HMM state identified by vbSPT. Lastly, a Gaussian mixture model (GMM) was used to cluster trajectories into free and bound states (Extended Data Fig. 2e,f and Supplementary Fig. 4). The standard deviations for the fraction of free and bound were determined by bootstrapping 100 times.

We compared diffusion coefficients of factors for their identified bound state (D_{bound}). Even though elongation factor Paf1 binds to elongating RNAPII, which could theoretically show higher D_{bound} due to 1D movement along the chromatin, our experiments show that its D_{bound} is similar to that of the histones. This suggests the observed D_{bound} in our experimental setup is predominantly influenced by the movement of chromatin itself, rather than by the 1D movement of the factor along it (Extended Data Fig. 1h,i).

Comprehensive explanation of multi-parameter classification—Single-molecule tracking experiments often yield transitioning trajectories, representing a mixture of multiple diffusive states. This presents a significant challenge in analyzing many chromatin-binding proteins in yeast, as their residence times are relatively short (approximately 5 seconds for chromatin remodelers[78] and PIC components[73]) and the observed trajectories often contain a mix of bound and free segments, with up to 30% of the total trajectories being state-transitioning trajectories for the chromatin remodeler ISW2[78]. Consequently, the overall diffusion characteristics become an average of free and bound states, perhaps contributing to a population displaying intermediate diffusion coefficients with apparent confined properties previously reported for TBP, TFIIA, TFIIB and TFIIE[73], when transitioning trajectories were not considered. In addition, the presence of these proteins in large protein complexes could also result in trajectories with intermediate diffusion coefficients. For example, a faction of diffusive TBP molecules is likely in complex with TAFs as TFIID[79], and TFIIB forms a holo-complex with poly(A) polymerase and the CF1[80].

Precise state determination is difficult for live cell experiments as trajectories obtained are typically short (Supplementary Fig. 2a). vbSPT employs a variational Bayesian hidden Markov model (HMM) to separate transitioning trajectories into multiple states according to displacement length distributions. The vbSPT algorithm uses the HMM to infer the most probable underlying state transitions, revealing information about the dynamic properties of the tracked particles[77]. However, unsupervised vbSPT can often overfit experimental data[81,82] (Extended Data Fig. 2a). The common approach, which we follow, is to conservatively categorize trajectories into two principal states: free and bound. This is supported by the diffusion coefficient histograms of chromatin-binding proteins, which typically exhibit two Gaussian peaks (Fig. 1b and Extended Data Fig. 1h).

In addition to the two principal states (free and bound), it might be tempting to further dissect the free state into fast (directed) and slow (confined) states, with the slow state potentially indicating entrapment or confinement. However, free trajectories can exhibit both fast and slow behavior due to the partial observation of inherent randomness, as demonstrated by Brownian simulation (Supplementary Fig. 2). Dissecting these free trajectories into specific states becomes more complex when a molecule does not consistently remain in one specific state for sufficient duration. Therefore, we typically adhere to a 2-state model, i.e. free and bound.

Population-based analyses such as Spot-On[83] and saSPT[84] allow the evaluation of trajectory diffusion coefficient distribution and the inference of overall population dynamics, while also compensating for defocalization and localization errors. However, these methods tend to overlook state transition, require data fitting to predefined diffusion models, and are unsuitable for spatiotemporal mapping, which requires the classification of individual tracks into specific states. To address these limitations, we have developed a multi-parameter classification pipeline using a track-based approach. The initial step involves applying a two-state hidden Markov model (HMM) to the single-molecule tracking data, effectively segregating the free and bound segments of all transitioning trajectories into distinct single-state trajectories (Extended Data Fig. 2b). Subsequently, we select 10 parameters, informed by literature[85–87] and introduce a novel parameter, ‘Angle Bias’, to characterize each trajectory with respect to diffusivity, geometry and angular orientation. An advantage of these parameters is their flexibility in fitting the trajectories’ properties without requiring a predefined diffusion model. Similar track-based methods have also recently emerged in the field, such as pEMv2[88], Bound2Learn[89] and diffusional fingerprinting[86].

10 parameters for multi-parameter classification:

1. **Diffusion coefficient (D)**: A measure of the molecular movement rate through a medium, calculated from the mean squared displacement (MSD) as a function of time:

$$D = MSD(\tau)/(4\tau)$$

τ is the time lag/interval. MSD is the average squared displacement a molecule moves from its initial position within a trajectory after a given τ. As molecular

diffusion in a complex biological system often deviates from simple Brownian diffusion, the diffusion coefficient was derived from the linear part of the MSD curve and should be considered as an 'apparent' diffusion coefficient.

2. **Alpha (α)**: Represents anomalous diffusion behavior in the trajectory, determined from the MSD scaling exponent as a function of time:

$$\mathrm{MSD}(\tau) \propto \tau^{\alpha}$$

τ is the time lag/interval. α describes the deviation from normal diffusion, where $\alpha = 1$ represents normal diffusion, $\alpha < 1$ indicates subdiffusion, and $\alpha > 1$ signifies superdiffusion (Supplementary Fig. 2b).

3. **Maximum displacement**: The largest Euclidean distance a molecule moves between any two consecutive steps within a trajectory.

4. **Minimum displacement**: The smallest Euclidean distance a molecule moves between any two consecutive steps within a trajectory.

5. **Mean displacement**: The average Euclidean distance a molecule moves between any two consecutive steps within a trajectory.

6. **Span**: The Euclidean distance between the initial and final positions of a molecule in a trajectory.

7. **Angle Bias**: A measure of the preferential directionality of a molecule's movement, calculated by a weighted average of the angles (θ) between consecutive displacements in the trajectory, with $0° \le \theta \le 180°$. Each angle is transformed into a score using the equation based on a bipolar sigmoid function:

$$\mathrm{Score} = \frac{1 - \frac{2}{1 + e^{\frac{90 - \theta}{\mathrm{weight}}}}}{1 - \frac{2}{1 + e^{\frac{90}{\mathrm{weight}}}}}$$

Weighted averaging emphasizes extreme angles, with the weight set to 20. Angle Bias value is 0 for normal diffusion, > 0 for forward bias, and < 0 for backward bias.

8. **Asymmetry 1**: A parameter quantifying the deviation from a symmetrical shape, typically represented by an ellipse of gyration[87]. Asymmetry 1 is computed using the radius of gyration tensor (T) for a 2D random walk. The principal radii of gyration (R1 and R2) are the eigenvalues of tensor T, where R1 corresponds to the larger principal radius and R2 to the smaller principal radius of gyration.

$$\mathrm{Asymmetry}\ 1 = \frac{(R1 - R2)^2}{(R1 + R2)^2}$$

The ratio ranges from 0 to 1, with 0 for circularly symmetric trajectories and 1 for linear trajectories.

9. **Asymmetry 2**: Orthogonal to Asymmetry 1[87],

$$\text{Asymmetry } 2 = \frac{R2}{R1}$$

The ratio ranges from 0 to 1, with 1 for circularly symmetric trajectories and 0 for linear trajectories.

10. **Aspect ratio**: The ratio between the long and short side of the minimum bounding rectangle. It is 1 for symmetric trajectories and becomes larger for elongated trajectories.

After calculating the 10 parameters for each trajectory, we apply Uniform Manifold Approximation and Projection (UMAP) for dimensionality reduction. This process is intended to separate the trajectory data into two distinct clusters, corresponding to the free and bound states. However, the UMAP projection may not always clearly differentiate these clusters. To refine this categorization, we enhance the separation of the two clusters by semi-supervision using the hidden Markov model (HMM) states identified by vbSPT (Extended Data Fig. 2c–f). Subsequently, we define the clusters using a Gaussian Mixture Model (GMM), and each trajectory is classified into one of two classes: class 1, representing the bound state, or class 2, representing the free state (Extended Data Fig. 2e–g).

Nucleoplasm/Nucleolus ratio—To calculate the ratio of freely diffusing molecules between the nucleoplasm and the nucleolus, we counted the number of localizations in both compartments and normalized these values with the respective areas of the nucleoplasm and the nucleolus. Standard deviations were determined by bootstrapping 100 times. We also carried out Brownian simulations to mimic the single-molecule random distribution for a specific nucleoplasm/nucleolus ratio, using custom-written scripts in R.

Spatiotemporal mapping—We transformed, normalized, and merged single-molecule localizations from multiple cell nuclei using the centroids of the nucleus and the nucleolus for reference. All yeast nuclei were in G1 phase, displaying distinct nuclear envelope and nucleolar boundaries to ensure that the single-molecule signals were measured on a similar 2D plane. In the 2D projections on an x-y axis, the left and right sides are defined by the position of the nucleolus, but the top and bottom remain unspecified due to the absence of landmarks for defining the angle around the central axis; therefore, mirroring around the central axis was necessary to facilitate visualization[36] (Supplementary Fig. 5b). Bins separated by 10 nm were applied across the nuclear area, each with a 150 nm detection radius, and the probability density was calculated based on the number of localizations within this radius (Extended Data Fig. 3b). The choice of the 10 nm bin distance was arbitrarily determined to ensure adequate data point coverage for constructing the heatmap (Extended Data Fig. 3c). Different detection radii were tested, and 150 nm was selected as it provided a suitable resolution for representing density differences across the nucleus (Extended Data Fig. 3c). The density of bound trajectories maps was normalized against

total localizations to highlight changes in the bound fraction, whereas density of free trajectories maps was normalized against total free localizations to emphasize confinement. Since the (probability) density value does not reflect the actual molecular density, we do not report specific values. Instead, we present qualitative changes using a divergent continuous spectral scale that transitions from cool colors (blues) for lower densities to warm colors for higher densities. This type of scale is designed to visually separate distinct ranges, enhancing the interpretability of density distributions; small changes in color intensity, especially within similar hues, may not necessarily indicate major differences in data but could reflect minor fluctuations or inherent noise within the dataset, and should be interpreted cautiously. Additionally, we provide an example with a monochromatic gradient scale in the Supplementary Fig. 5c for further visualization. It is important to note that the spatiotemporal maps are generated from single-molecule tracking movies; the density should be interpreted as the probability of finding a molecule in that position over time, rather than instantaneous protein clustering. Thus, the physical dimensions and shapes of these probability patterns should not be over-analyzed.

Our study typically used 10–20 aligned nuclei, generating at least 1,000 trajectories with a median of 8–10 steps (Supplementary Fig. 2a). As a result, our dataset contains approximately 100,000 data points. For instance, in wildtype RNAPII (Fig. 2e), the bound and free maps contain 66,586 and 35,727 localizations, respectively. Supplementary Fig. 5a demonstrates that subsampling either half or a quarter of the data from the RNAPII bound map into three random samples produces essentially identical maps. The map pattern only becomes unstable when the data is reduced by 50-fold, dropping to around 1,000 data points. This indicates the number of data points per dataset is sufficient to generate a statistically sound map pattern.

For genome simulation maps, we utilized 3D genome simulation data from yeast interphase chromosomes[37] (Extended Data Fig. 3d), disregarding the z-axis information, projecting the genome coordinates onto a 2D plane using orthographic projection. Sequence coordinates from the Saccharomyces Genome Database (SGD) were integrated with data on highly expressed genes across multiple gene classes[41,63], as identified in minimal medium[38], to illustrate their probability density distributions on a 2D map (Fig. 1d). It is important to note that such simulations inherently include gene loci from both the top and bottom of the 3D volume in the same 2D representation, leading to conflated gene loci representations in the 2D plane. While these simulations provide valuable insights, they should be interpreted with caution and regarded as a supplemental frame of reference to aid in understanding our spatiotemporal maps, rather than as definitive representations of 3D genomic arrangements.

We anticipated that the detection of bound trajectories in single-molecule experiments would likely be biased towards genes that are highly expressed; hence, we selected only highly expressed genes from multiple classes for the genome simulation. Similar to the construction of the spatiotemporal map, mirroring around the central axis was conducted. Consequently, genes located on the opposite side along the central axis might appear in close proximity. Therefore, this density visualization represents the probability density of gene locations within specific classes in defined regions, rather than actual instantaneous gene clustering. Additionally, we present a genome simulation map for total genomic DNA, which mimics

the Rabl configuration of yeast chromosomes. Importantly, the genome simulation map represents only a snapshot of a single thermodynamically stable configuration of the genome and ignores the dynamic nature of chromosomes in the living cell, as well as the variation between individual cells.

Anisotropy ($f_{180/0}$) analysis—We isolated the free trajectories in the nucleoplasm by multi-parameter classification, and extracted the angles between two displacements for analysis. We subsampled the trajectories to obtain angles for a total of 30 time intervals. Next, we identified anisotropy by comparing the change of $f_{180/0}$ (fraction of 180° ± 30° over 0° ± 30°) across various length scales of mean displacement (the mean of the two displacements generating the angle)[44]. We restricted our examination to mean displacements of 350 nm or less, given the small size of yeast nuclei and the apparent anisotropy for longer displacements due to nuclear confinement (Extended Data Fig. 6a,b). Standard deviations were determined by bootstrapping 100 times. Misclassifying bound segments as free displacements or having state-transitioning trajectories could significantly increase the $f_{180/0}$ value[44]. We found that our multi-parameter approach outperformed the original vbSPT approach[44] in classifying free and bound displacements for our yeast data (Extended Data Fig. 2b,d,f). In scenarios with increased bound fraction, misclassifying bound displacements as free would increase the anisotropy observed in the free population. In the *ssn3Δ* experiment, our data show an increased RNAPII bound fraction without a corresponding increase in anisotropy (Extended Data Fig. 7h,i), validating our classification for free and bound displacements. In addition, a moderate decrease in Mediator binding (Rgr1-Halo and Med1-Halo) observed in the CTD9 mutant (Fig. 6a,b) prompted us to examine if this could account for the observed RNAPII-CTD9 dynamics (Fig. 2 and 3). Despite the restoration of Mediator binding (Rgr1-Halo) in a strain co-expressing $RPB1^{Rpo21}$-CTD26 (WT) and $RPB1^{Rpo21}$-CTD9 (Extended Data Fig. 7e), RNAPII-CTD9 consistently exhibited a significant decrease in bound fraction (Extended Data Fig. 7f) and near-isotropic diffusion (Extended Data Fig. 7g). This suggests that the changes in RNAPII dynamics are more likely intrinsic to the CTD truncation, rather than being predominantly driven by the decreased Mediator binding.

Slow-tracking data analysis

Measurement of residence time—In contrast to fast tracking, we accounted for blinking or transient defocalization of bound molecules by allowing gaps of up to one frame between two localizations. We linked them as one trajectory if they were less than three pixels (r_{max} = 321 nm) apart. This is the upper threshold for the displacements between two successive frames, and 98% of the bound RNAPII, H2B, H3 and H2A.Z displacements were below this threshold (Extended Data Fig. 8e). A survival curve (1-CDF) against time was plotted and fitted with a double exponential decay model:

$$P(t) = f_{sb}e^{-k_{sb}t} + f_{tb}e^{-k_{tb}t}$$

Here, k_{sb} and k_{tb} represent dissociation rates for stable- and transient-binding events, respectively, and $1 = f_{sb} + f_{tb}$ for the fraction of the two components. We do not interpret transient binding as binding to non-specific sites, but rather as a neutral description of the

binding duration. The residence times observed are typically underestimated due to factors such as chromatin movements and photobleaching. We use the dissociation rates of stably bound H2B as a control to correct apparent dissociation rates[47] (Extended Data Fig. 8f). Given that fluctuations in the microscope setup could result in variable photobleaching rates, we routinely image H2B and the protein of interest on the same day[47,78]. To further overcome technical fluctuations, we spike the imaging culture with Halo-H2B cells harboring a labeled nuclear marker Pus1-miRFP670nano3, and co-image the two strains in the same field of view (Fig. 5a).

The corrected decay constant was obtained as $k_{corrected} = k_{observed} - k_{sb,H2B}$, and the corrected residence time is its inverse. Standard deviations were determined by bootstrapping 10,000 times. The stably bound fraction was calculated by multiplying the fraction bound from fast tracking with the fraction of stably bound (f_{sb}) in slow tracking. For CTD9 experiments, we used Halo-H2B cells in CTD9 background for correction. The values of $k_{sb,H2B}$ between CTD9 and WT are comparable (Extended Data Fig. 8g,h).

Measurement of search time—Search time is the average duration for a molecule to move between stably binding sites (Fig. 5f), accounting for the time and fraction spent in stably bound, transient bound, and free states, as inferred from fast and slow tracking data. Detailed calculations and explanations can be found in previous study[73]. A limitation of this approach is the difference in exposure time used in fast and slow tracking (10 ms/frame versus 250 ms/frame), as slow tracking may not capture exceedingly transient binding events due to its long frame rate. Nevertheless, the estimated search time remains a useful metric for evaluating changes in search kinetics in different mutants and experimental conditions.

Stochastic optical reconstruction microscopy (STORM)

Yeast expressing HaloTag fusion proteins were labeled with equal concentrations of JF552 and JFX650, incubated for 4 hours, and either fixed in 4% PFA or imaged as live cells. Image acquisition was conducted using ~1 kW/cm^2 of 555 nm and 637 nm laser power, 80 ms/frame, and lasted 5–10 minutes for fixed cells or 5 minutes for live cells. W-VIEW GEMINI enabled simultaneous two-color imaging. Channels were manually aligned, and data were corrected for drift and chromatic aberration using the DoM plugin in ImageJ[79]. For fixed cell experiments, fluorophore blinking was removed by pairwise distance distribution correction (DDC)[80].

HaloTag bulk staining

Yeast expressing HaloTag fusion proteins were labelled with 100 nM of JFX650 in live cell for 4 hours. Image acquisition was conducted using a 637 nm laser at low power. Z-stacks of wide-field images, each consisting of nine slices with a z-interval of 0.3 μm, were captured. Intensity was calculated using average intensity projection. Beam intensity across the field of view was recorded using a fluorescence slide to rectify distortions caused by Gaussian-shaped beam illumination.

Auxin-induced degradation (AID)

Auxin-induced degradation (AID)[81] of endogenous RPB1^{Rpo21} or MED14^{Rgr1} was achieved by tagging the target protein with AID*-miRFP670nano3 in strain expressing F-box proteins OsTIR1 and AtAFB2 (Extended Data Fig. 5j). Imaging culture was pre-incubated with auxin (I5148; MilliporeSigma, Germany) at a final concentration of 0.5 mM for an hour, and culture was maintained in auxin-medium throughout imaging. Degradation of target protein was confirmed by the depletion of miRFP670nano3 fluorescence signal in living cells (Fig. 3h and Extended Data Fig. 5e,f). To minimize the potential photodestruction of auxin and the generation of related toxic derivatives by strong laser exposure[82], the medium was replaced with fresh auxin medium every 10 minutes during imaging. For the '−Auxin' control, DMSO was used as a substitute for auxin. To further rule out the potential side-effect of auxin, we added auxin to cells expressing ectopic RPB1^{Rpo21}-Halo in an RPB1^{Rpo21} AID background. The changes in the bound fraction and $f_{180/0}$ of RNAPII were minimal compared to those in the WT (Extended Data Fig. 5g,h).

Heat shock

Cells were subjected to heat shock by washing with 39°C SC medium twice in the imaging chamber, then immediately transferring to a preheated 39°C stage-top incubation chamber (Okolab) for imaging.

Measuring transcription bursting of *HSP82*

Live-cell transcription imaging was performed on 24xPP7-*HSP82* yeast strains expressing a fusion protein consisting of mScarlet-Ix3 and a non-aggregating ΔFG mutant[83] of the dimerized PP7 coat protein (PP7CPx2-mScarlet-Ix3). Z-stacks of wide-field images, each consisting of nine slices with a z-interval of 0.5 μm, were captured every 20 seconds for 40 minutes, using 150 ms exposure with a 555 nm laser at ~0.005 kW/cm^2. At least four replicates were acquired per condition, with a minimum of 100 cells showing transcription site signals in total.

Maximum intensity projected images were drift-corrected, and nuclei were manually inspected for presence of transcription sites. Cells undergoing division were excluded from the analysis. Single-frame bursts were removed, and bursts separated by just one frame were merged[84]. To calculate average ON and OFF times, the cumulative distribution functions (CDFs) of the respective time distributions were fitted with gamma and Weibull distributions, respectively[85]. Standard deviations were determined by bootstrapping 10,000 times.

Protein extraction and Western blotting

Protein extraction was performed using the LiAc/NaOH method[86], followed by SDS-PAGE separation. Proteins were transferred to a PVDF membrane (Bio-rad, USA) using a TE 70 PWR Semi-dry Transfer Unit (GE Healthcare, USA). Blots were blocked with 5% nonfat milk in TBST (Tris-buffered saline with 0.05% Tween 20) for 1 hour at room temperature, incubated with anti-CTD antibody (1:2000; 8WG16; MilliporeSigma, Germany) in 5% nonfat milk in TBST at 4°C overnight, and then with anti-mouse IgG-HRP (NA931; GE Healthcare, USA) in TBST for 1 hour at room temperature. Blots were developed using

ECL Prime Western blotting detection reagent (GE Healthcare, USA) and detected on an ImageQuant™ LAS 4000 biomolecular imager (GE Healthcare, USA).

Statistics and reproducibility

Statistical analyses were performed using GraphPad Prism (version 9.4.0) or RStudio (version 2021.09.1+372; R (version 4.1.2)). Values are mean ± s.d. unless otherwise stated. Significance levels: * $P \leq 0.05$, ** $P \leq 0.01$ and *** $P \leq 0.001$; ns, not significant. Statistical tests and P values are reported in figure legends. For reliable fitting and statistical evaluation, data obtained from at least two independent imaging sessions were resampled by bootstrapping (100 times for fast tracking, and 10,000 times for slow tracking). Representative microscopic images and Western blot from at least two independent acquisitions are shown in the figures.

Extended Data

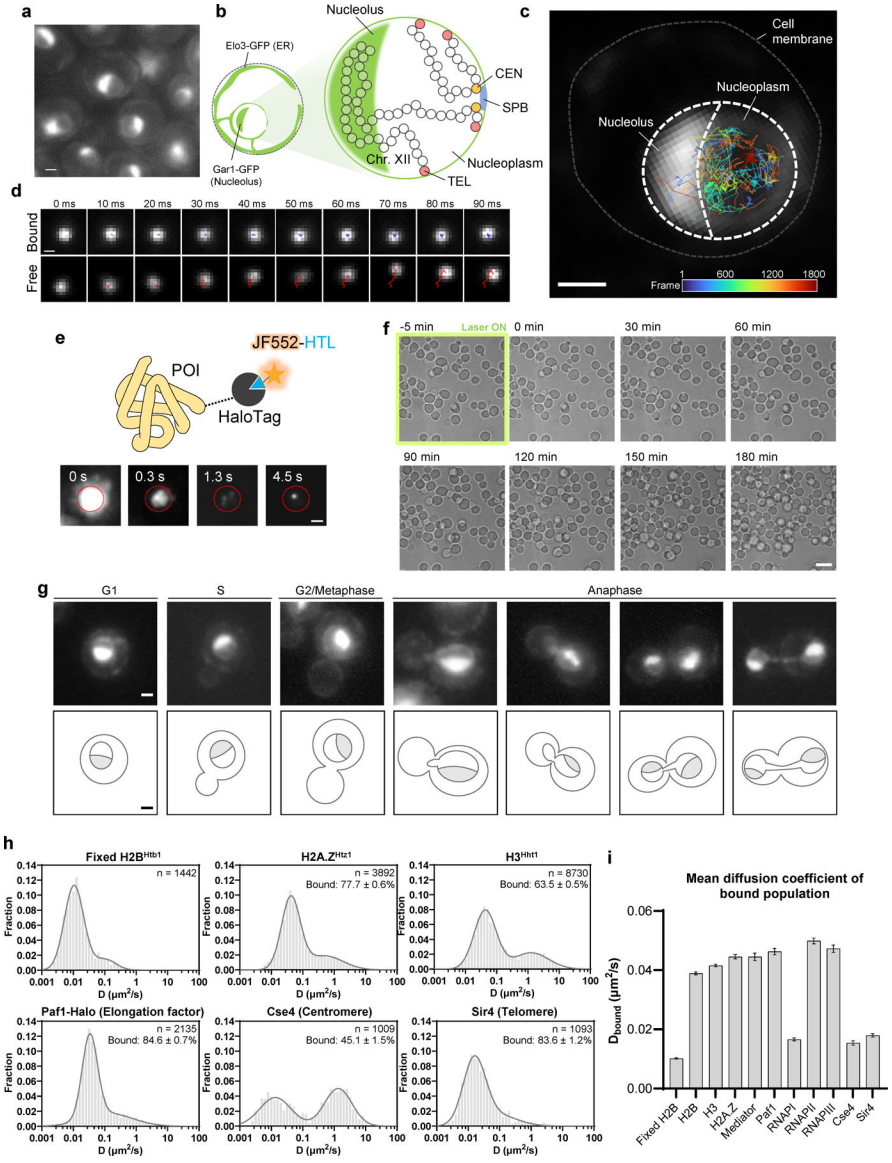

Extended Data Fig. 1. Single-molecule tracking in living yeast.

a, ER and nucleolus shown by Elo3-GFP and Gar1-GFP. Scale bar: 1.0 μm. **b**, Coarse-grained representation of yeast interphase chromosomes, physically constrained by telomere (TEL)-nuclear envelope and centromere-spindle pole body (CEN-SPB) tethering. **c**, Overlay of RPB1^{Rpo21}-Halo^{JF552} trajectories on the nucleus relative to ER and nucleolar GFP markers. Rainbow colors indicate the first appearance of each trajectory. Scale bar: 1 μm. **d**, Single-molecule trajectories of RPB1^{Rpo21}-Halo^{JF552} (free or bound) with diffusion coefficients. Scale bar: 0.2 μm. **e**, Protein of interested (POI) fused with HaloTag, labeled with JF552-HaloTag ligand (JF552-HTL) (top). Initial laser exposure of JF552 resulted in strong ‘nuclear glow’, followed by shelving in dark state and stochastic reactivation, leading to single-molecule detection. Nucleus circled in red. Scale bar: 1.0 μm. (bottom). **f**, Strong 555 nm laser exposure for 5 min does not result in noticeable cell death or growth arrest.

Scale bar: 4.0 μm. **g**, ER and nucleolar GFP markers for cell cycle stage identification. Scale bar: 1.0 μm. **h**, Diffusion coefficient histograms of various nuclear proteins (n: number of trajectories; mean value ± s.d.). **i**, Assessing the mean diffusion coefficients of the bound population reveals no significant difference between histones (H2B, H3 and H2A.Z) and proteins that can move along DNA (e.g. RNAPII, RNAPIII, Paf1), while nucleolar RNAPI, and proteins that are physically tethered (Cse4 and Sir4) have significantly lower values (n = 100 resamplings; mean value ± s.d.). Source numerical data are available in source data.

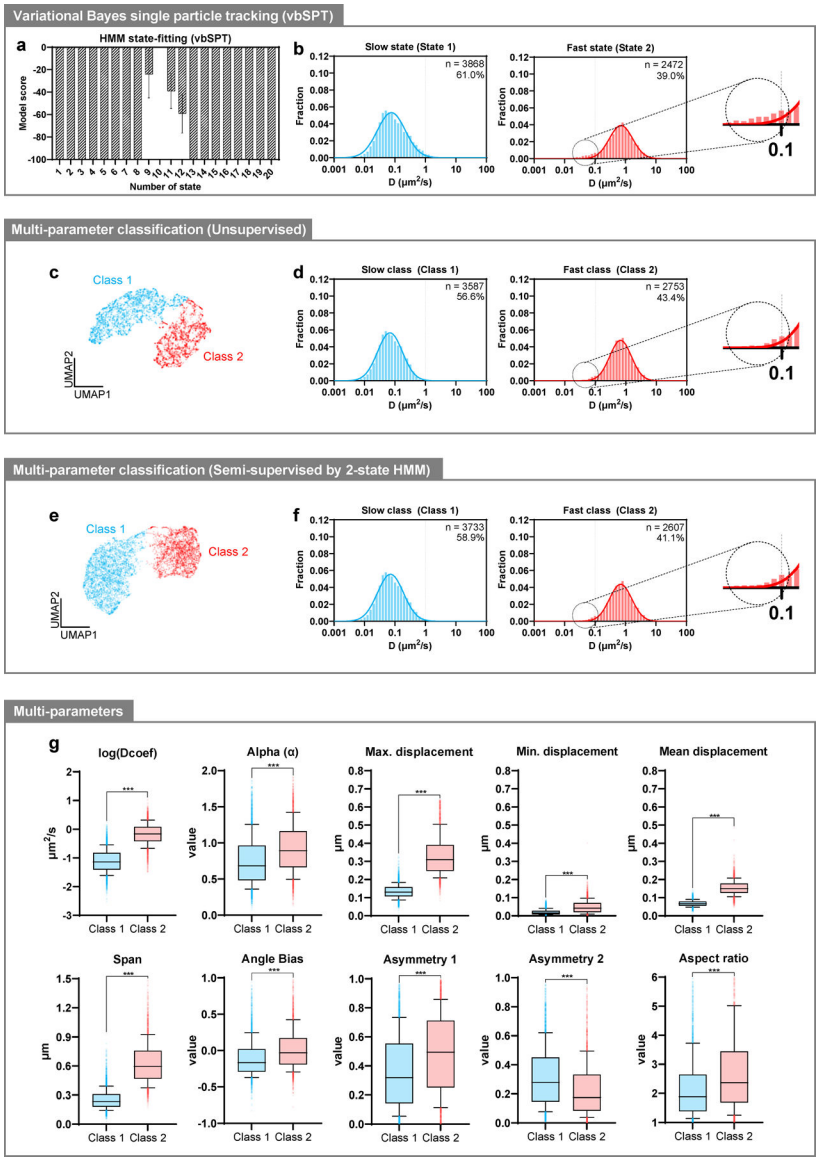

Extended Data Fig. 2. Multi-parameter classification of trajectories.

a, Unsupervised vbSPT overfits SMT data of RNAPII (n = 100 resamplings; mean value ± s.d.). **b**, Diffusion coefficient histogram for fast and slow states from 2-state HMM using vbSPT. A minor fraction of very slowly diffusing trajectories was misclassified as fast-state (dashed circle) (n: number of trajectories; mean value ± s.d.). **c**, Unsupervised

multi-parameter classification of RNAPII trajectories with UMAP dimensionality reduction and GMM clustering. **d**, Diffusion coefficient (D) distribution for the classified clusters (n: number of trajectories; mean value ± s.d.). **e-f**, similar to **c-d**, but with multi-parameter classification semi-supervised by 2-state HMM. **d** and **f**, Compared to **b**, Fast-class diffusion coefficient distribution showed less tailing (dashed circle). **g**, 10 parameters used for classification and their distributions in identified classes (n = 3733 trajectories for class 1 and n = 2607 trajectories for class 2; median (line), IQR (box), 10–90 percentile (whiskers) and outliers (crosses); two-tailed unpaired t-test, *** $P < 0.000000001$). Source numerical data are available in source data.

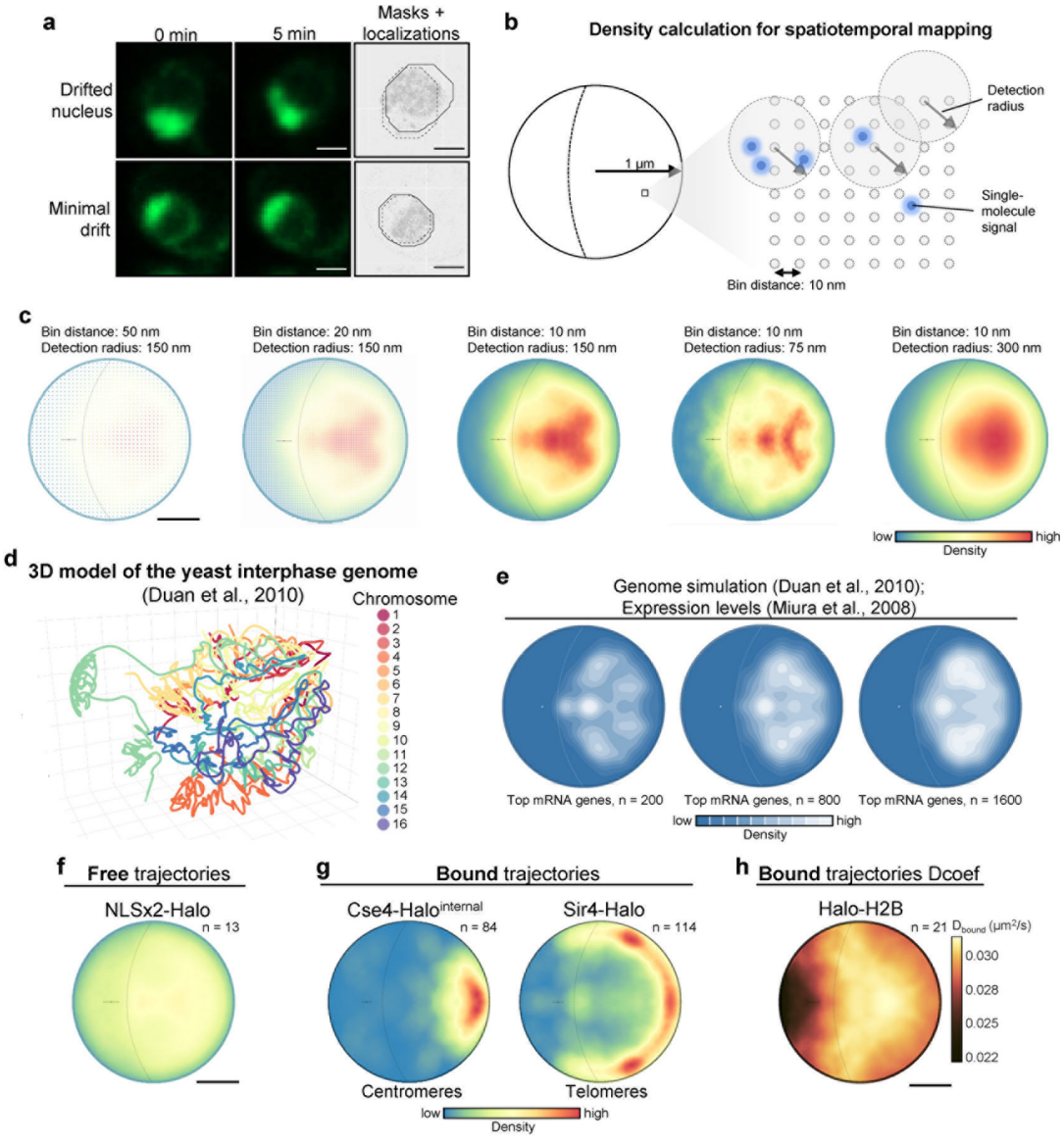

Extended Data Fig. 3. Spatiotemporal mapping reveals dynamics of nucleosome and nuclear landmark proteins.

a, Nuclei in G1 cells with minimal drift selected for spatiotemporal mapping. Scale bar: 1.0 μm. **b**, Localization density calculated using 150 nm detection radius from bins

separated by 10 nm. **c**, 150 nm detection radius and bin distance of 10 nm provide optimal coverage and resolution for the density on the bound map of RNAPII. Scale bar: 0.5 μm (n = 15 cells; Error bar: centroid of nucleolus ± s.d.). **d**, 3D simulation of the yeast interphase genome based on 3C data[37]. **e**, Top mRNA genes simulation maps based on gene expression data in minimal medium[38]. Left panel is reuse of Fig. 1d top panel (n: number of genes). **f**, Freely diffusing NLSx2-Halo map. Scale bar: 0.5 μm (Error bar: centroid of nucleolus ± s.d.; n: number of nuclei). **g**, Bound Cse4 (left) and Sir4 (right) maps (Error bar: centroid of nucleolus ± s.d.; n: number of nuclei). Sir4 bound map showed dense regions proximal and distal to the centromere, mirroring the telomere clusters of short and long chromosomes[35,37,65]. **h**, Bound H2B diffusion coefficient map. A 300 nm detection radius was used. Scale bar: 0.5 μm (Error bar: centroid of nucleolus ± s.d.; n: number of nuclei). Telomere and centromere movements are confined due to attachment to the nuclear envelope and spindle pole body, respectively[66]. Likewise, the local diffusion coefficients of chromatin-bound H2B reveal lower histone dynamics near centromeres and telomeres (Extended Data Fig. 1h,i).

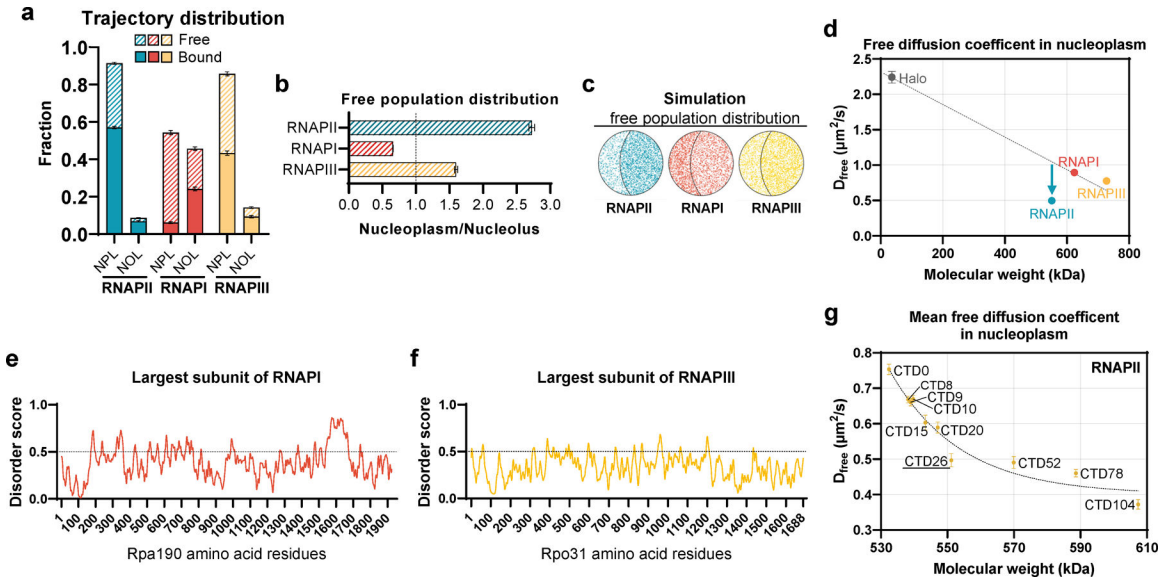

Extended Data Fig. 4. Spatiotemporal dynamics of RNAPII, RNAPI and RNAPIII.

a, Fraction of free and bound in nucleoplasm (NPL) and nucleolus (NOL) (n = 100 resamplings; mean value ± s.d.). **b**, Distribution (area normalized) of free RNAPII, RNAPI and RNAPIII in nucleoplasm and nucleolus (n = 100 resamplings; mean value ± s.d.). **c**, Simulation of Nucleoplasm/Nucleolus distribution. **d**, Diffusion coefficients and molecular weights of free RNAPII, RNAPI and RNAPIII in nucleoplasm (n = 100 resamplings; mean value ± s.d.). **e**-**f** IUPRED3 disorder scores for the largest subunit of **e**, RNAPI (Rpa190) and **f**, RNAPIII (Rpo31). Residues with predicted scores above 0.5 considered disordered. **g**, D_{free} of RNAPII and CTD mutants in nucleoplasm (n = 100 resamplings; mean value ± s.d.). Source numerical data are available in source data.

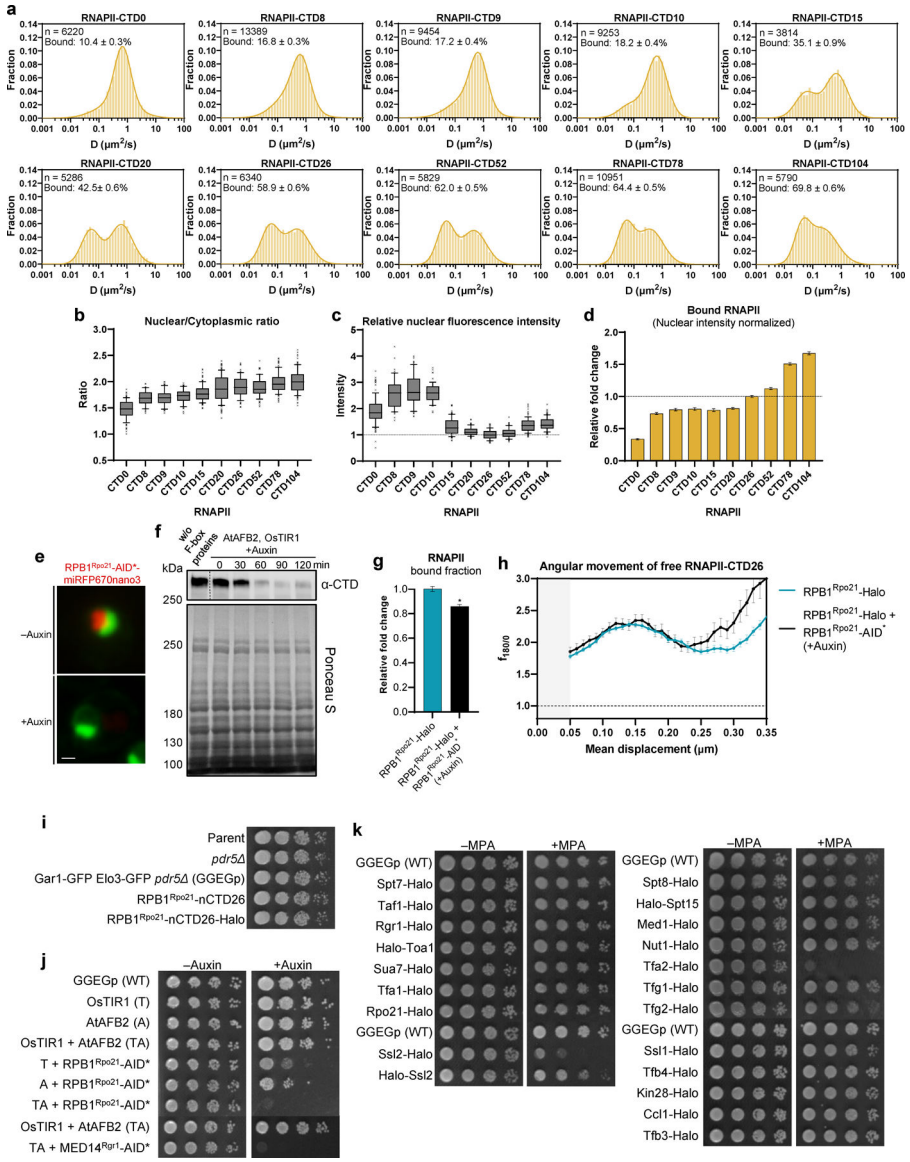

Extended Data Fig. 5. CTD length affects RNAPII subcellular distribution and expression.

a, Diffusion coefficient histogram for RNAPII with varying CTD lengths (n: number of trajectories; mean value ± s.d.). **b**-**c**, **b**, nuclear/cytoplasmic ratio and **c**, relative nuclear intensity of WT RNAPII and CTD mutants (median (line), IQR (box), 10–90 percentile (whiskers) and outliers (crosses), n = 95 nuclei for CTD0, 52 nuclei for CTD8, 69 nuclei for CTD9, 64 nuclei for CTD10, 112 nuclei for CTD15, 108 nuclei for CTD20, 69 nuclei for CTD26, 73 nuclei for CTD52, 91 nuclei for CTD78, 102 nuclei for CTD104). CTD truncation led to increased cytoplasmic and nucleolar distribution, and overexpression of RNAPII. **d**, Amount of bound RNAPII normalized to nuclear fluorescence intensity (n = 100 resamplings; mean value ± s.d.). The normalized value is an approximation, as the relationship between nuclear fluorescence intensity and RNAPII levels may not be strictly linear. **e**, Fluorescence signal of RPB1^{Rpo21}-AID*-miRFP670nano3 (red) before and after RNAPII degradation by auxin. Nucleolar and ER markers in green. Scale bar:

1.0 μm. **f**, Western blot showing time course degradation of RPB1^{Rpo21}-AID* by auxin, detected using CTD antibody (top), and Ponceau S staining on total protein (bottom). **g-h**, Cells expressing ectopic RPB1^{Rpo21}-Halo in an RPB1^{Rpo21} AID background show minimal changes in the **g**, bound fraction (n = 100 resamplings; mean value ± s.d.; two-tailed unpaired t-test, * $P = 0.015275$) and **h**, $f_{180/0}$ of RNAPII after auxin treatment, compared to those in WT expressing RPB1^{Rpo21}-Halo (n = 100 resamplings; mean value ± s.d.). **i**, Spot assay for strains with *prd5Δ*, GFP markers (GGEGp), RPB1^{Rpo21}-nCDT26, or RPB1^{Rpo21}-nCDT26-Halo showing identical growth. **j**, Spot assay demonstrating impaired cell growth for RPB1^{Rpo21} or MED14^{Rgr1} AID degron. All AID* constructs contain miRFP670nano3 as a fluorescence marker. **k**, Spot assay for strains with HaloTag fusions to various PIC component subunits to assess MPA sensitivity. Ssl2-Halo (TFIIH), Halo-Ssl2 (TFIIH), Tfa2-Halo (TFIIE), Tfg2-Halo (TFIIF) exhibited MPA sensitivity. Source numerical data and unprocessed blots are available in source data.

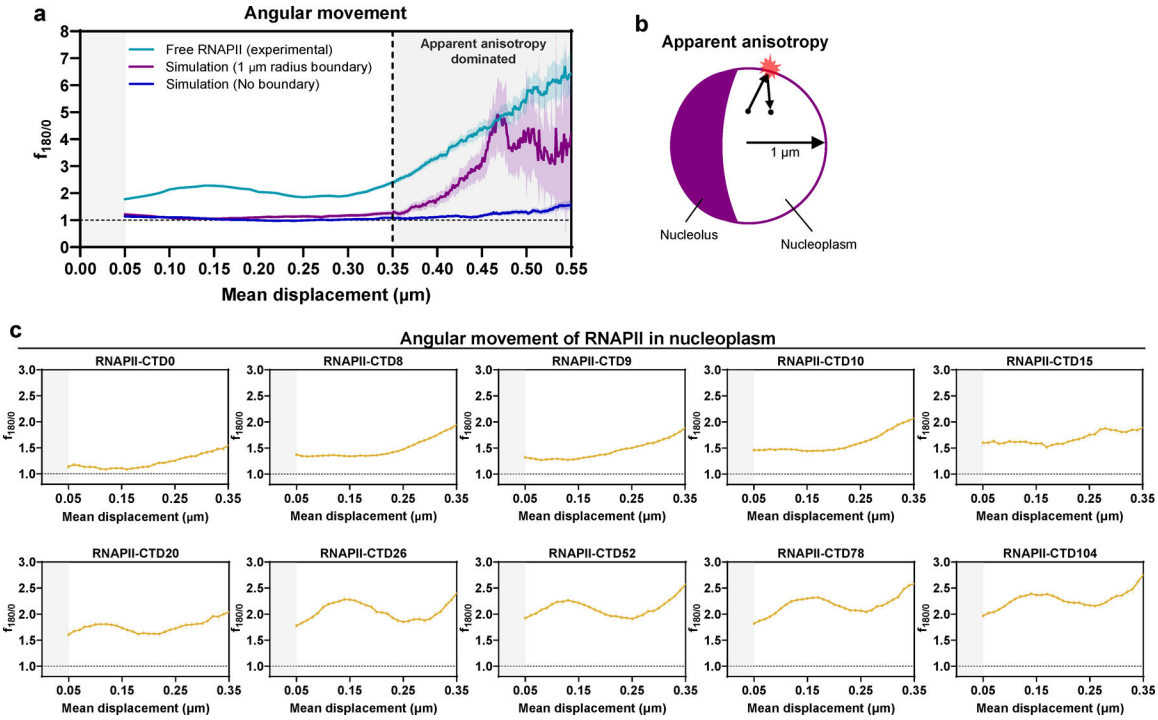

Extended Data Fig. 6. CTD length impacts free RNAPII anisotropy.

a, Brownian simulations indicate significant apparent anisotropy for mean displacement longer than 350 nm (n = 100 resamplings; mean value ± s.d.). **b**, Apparent anisotropy due to nuclear confinement in small yeast nucleus. **c**, CTD length increase leads to an elevation in $f_{180/0}$ trend (n = 100 resamplings; mean value ± s.d.). Source numerical data are available in source data.

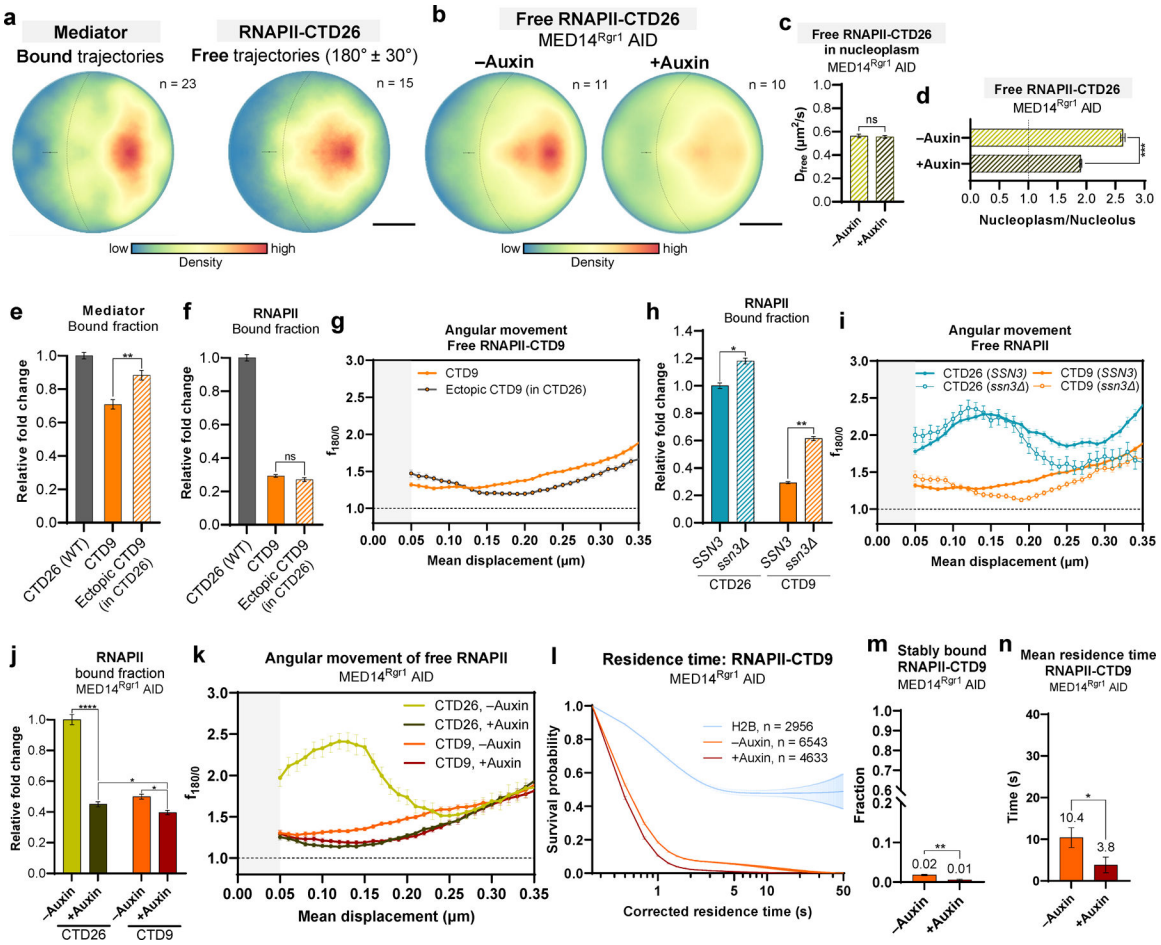

Extended Data Fig. 7. Investigating the role of Mediator in spatiotemporal confinement of RNAPII.

a, Bound Mediator map (left). Free RNAPII-CTD26 map showing confined trajectories (right). Scale bar: 0.5 μm. (Error bar: centroid of nucleolus ± s.d.; n: number of nuclei). **b**, Free RNAPII-CTD26 map in MED14^{Rgr1} AID. Scale bar: 0.5 μm (Error bar: centroid of nucleolus ± s.d.; n: number of nuclei). **c**-**d**, **c**, D_{free} in nucleoplasm (n = 100 resamplings; mean value ± s.d.; two-tailed unpaired t-test, ns $P = 0.510991$) and **d**, Nucleoplasm/Nucleolus of RNPAII-CTD26 in MED14^{Rgr1} AID (n = 100 resamplings; mean value ± s.d.; two-tailed unpaired t-test, *** $P = 0.000008$). **e**-**g**, **e**, Mediator bound fraction (n = 100 resamplings; mean value ± s.d.; two-tailed unpaired t-test, ** $P = 0.006771$), **f**, RNAPII bound fraction (n = 100 resamplings; mean value ± s.d.; two-tailed unpaired t-test, ns $P = 0.157495$) and **g**, $f_{180/0}$ for RNAPII-CTD9 in CTD26 background (n = 100 resamplings; mean value ± s.d.). **h**-**i**, **h**, Relative bound fraction (n = 100 resamplings; mean value ± s.d.; two-tailed unpaired t-test, * $P = 0.012696$, ** $P = 0.001329$) and **i**, $f_{180/0}$ for RNAPII-CTD26 and RNAPII-CTD9 in WT and *ssn3Δ* (n = 100 resamplings; mean value ± s.d.). Deleting Cdk8^{SSN3} from the Mediator kinase module[67–69] enhances interaction between the Mediator and RNAPII without changing free RNAPII confinement. **j**-**k**, **j**, Relative bound fraction (n = 100 resamplings; mean value ± s.d.; two-tailed unpaired t-test, * $P \leq 0.05$ and *** $P \leq 0.001$. Comparison between before and after auxin treatment: $P = 0.000014$

for CTD26 and $P = 0.0222222$ for CTD9. Comparison between CTD26 and CTD26 after auxin treatment: $P = 0.034745$) and **k**, $f_{180/0}$ (n = 100 resamplings; mean value ± s.d.) for RNAPII-CTD26 and RNAPII-CTD9 in MED14^{Rgr1} AID. **l-n**, **l**, Survival probability of H2B-corrected residence times (n = 10,000 resamplings; mean value ± s.d.), **m**, stably bound fractions (n = 10,000 resamplings; mean value ± s.d.; two-tailed unpaired t-test, ** $P = 0.002245$) and **n**, mean residence times (n = 10,000 resamplings; mean value ± s.d.; two-tailed unpaired t-test, * $P = 0.019928$) for RNAPII-CTD9 in MED14^{Rgr1} AID. Source numerical data are available in source data.

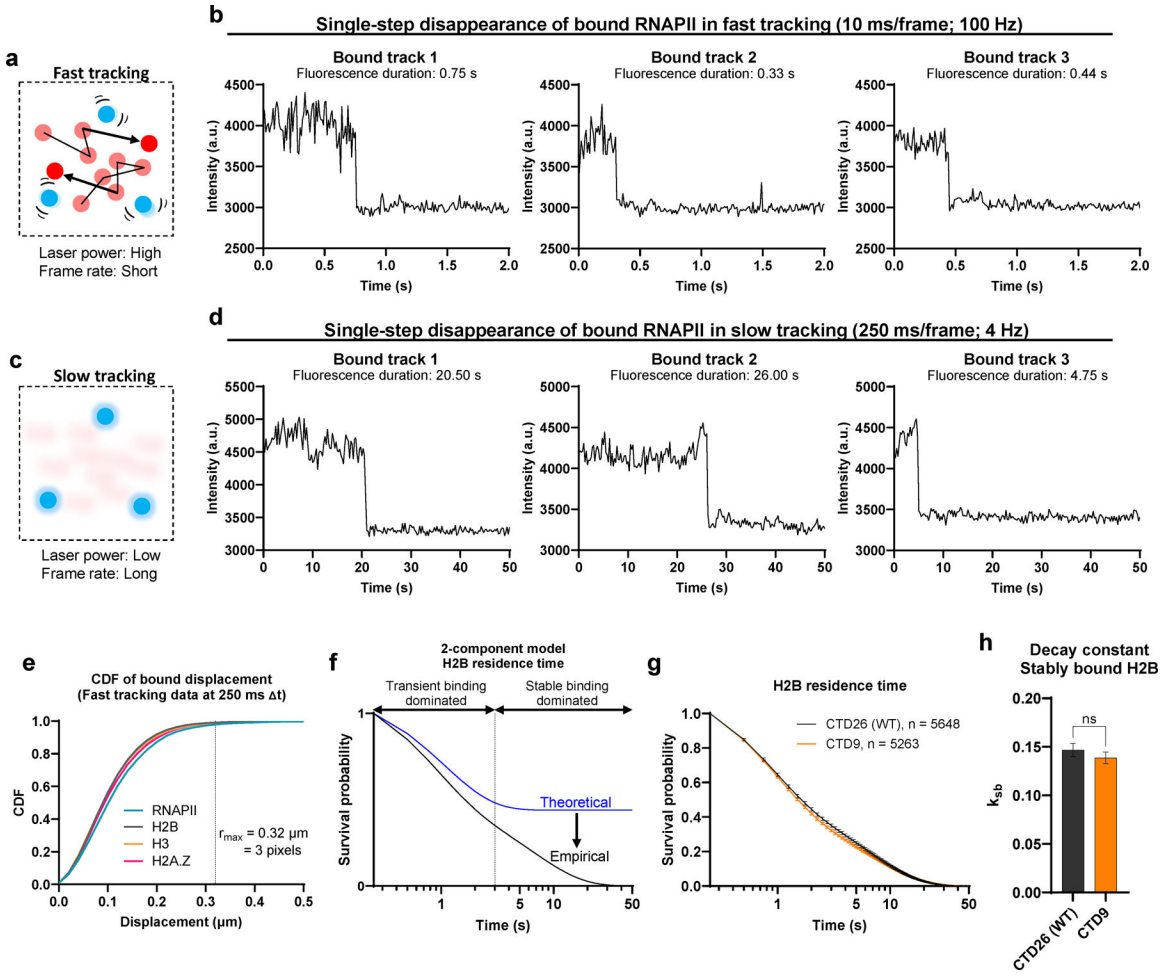

Extended Data Fig. 8. Fast and slow tracking mode of single-molecule tracking.

a, Fast tracking with high laser power and short frame rate (10 ms/frame) reveals diffusive dynamics of free (red) and bound (blue) molecules. **b**, Single-step disappearance of chromatin-bound RNAPII in fast tracking. **c**, Slow tracking with low laser power and long frame rate (250 ms/frame) reveals residence time of bound molecules (blue). **d**, Single-step disappearance of chromatin-bound RNAPII in slow tracking. **b-d**, Here we term 'disappearance' as we cannot definitively differentiate between the molecule diffusing out of the focal plane or photobleaching within the living cell. **e**, CDF of bound displacement of RNAPII, H2B, H3 and H2A.Z to determine the r_{max} for trajectory

linking in slow tracking[70]. **f**, In G1 cells, nucleosomal H2B (representing the stable binding population) was hypothesized to bind for a sufficiently long period, such that during image acquisition, their dissociation was barely observed. Nonetheless, the observed residence times for H2B typically fall within 30 seconds, due to factors such as photobleaching, dye blinking, chromatin/nuclear movements, and focus drift. **g**, Survival probability of Halo-H2B observed residence times in CTD26 (WT) and CTD9 strains (n: number of trajectories; mean value ± s.d.). **h**, Decay constant of stably bound Halo-H2B (k_{sb}) in CTD26 (WT) and CTD9 strains (n = 10,000 resamplings; mean value ± s.d.; two-tailed unpaired t-test, ns P = 0.339598). Source numerical data are available in source data.

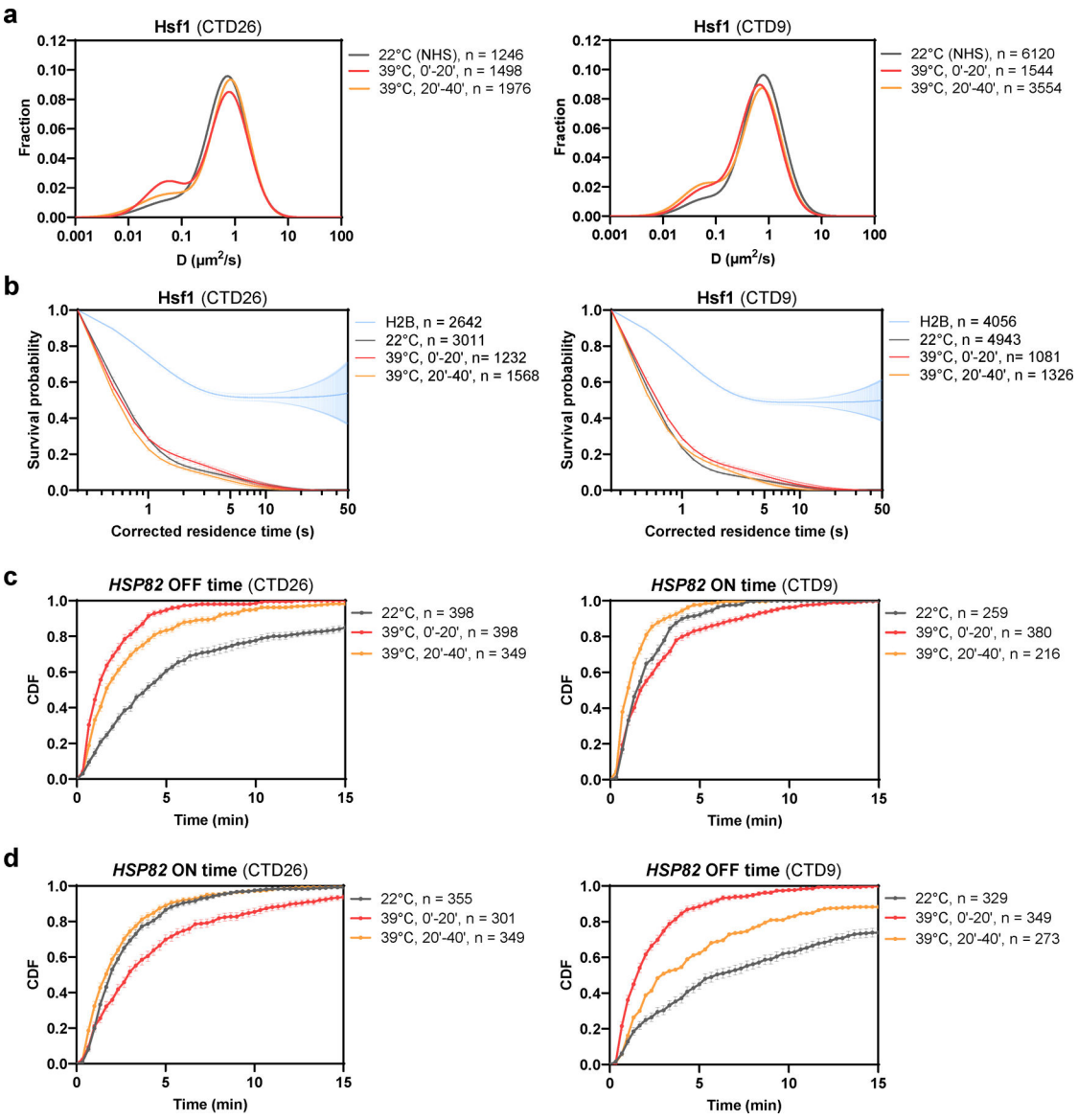

Extended Data Fig. 9. CTD length controls *HSP82* transcription bursting, with minimal effect on Hsf1 dynamics.

a-b, a, Diffusion coefficient histograms for Hsf1-Halo and **b**, survival probability of bound Hsf1-Halo under heat shock in CTD26 (WT) (left) and CTD9 (right) strains (n: number

of trajectories; mean value ± s.d.). **c-d, c**, *HSP82* ON time and **d**, OFF time cumulative distribution function (CDF) under heat shock in CTD26 (WT) (left) and CTD9 (right) strains (n: number of ON or OFF events; mean value ± s.d.). Source numerical data are available in source data.

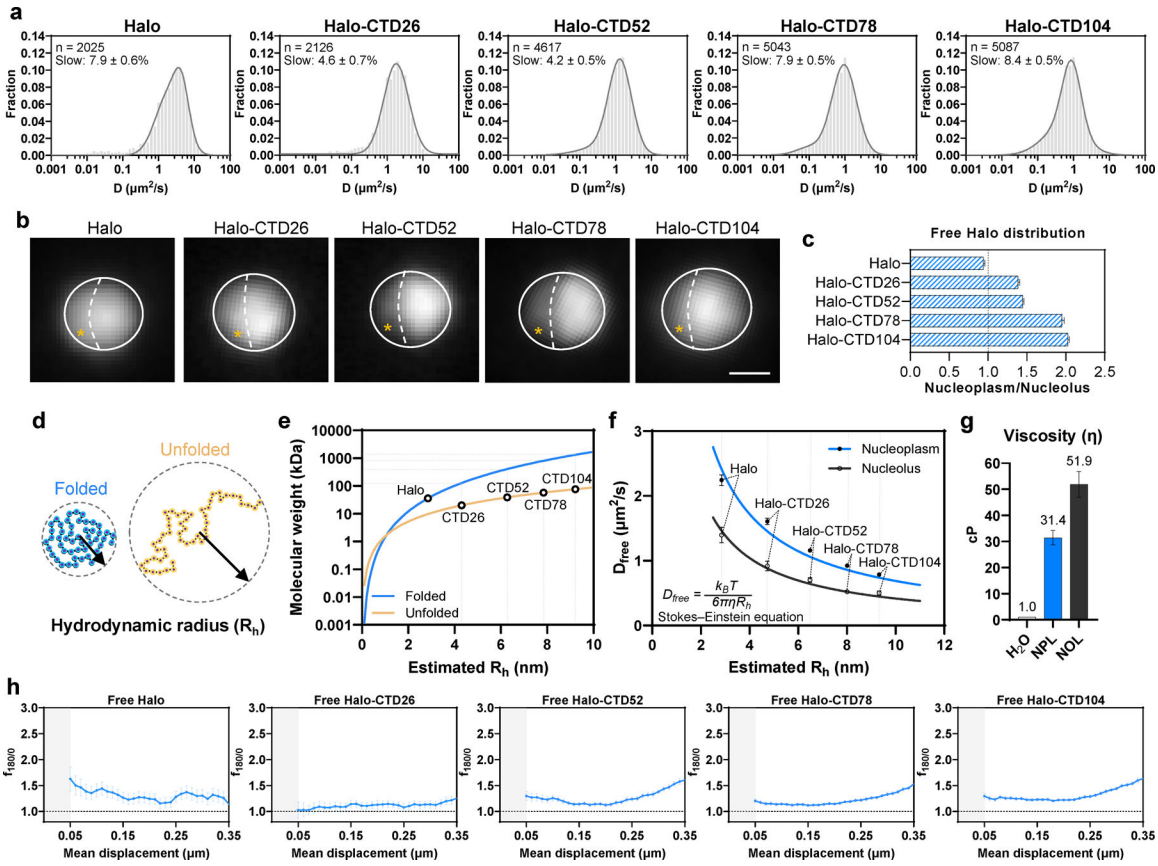

Extended Data Fig. 10. CTD is necessary but not sufficient for confining protein diffusion.

a, HaloTag (NLSx2-Halo) and Halo-CTD fusions diffusion coefficient histogram by CTD length (n: number of trajectories; mean value ± s.d.). The first plot is reuse of the top panel's second plot from Extended Data Fig. 1h. **b**, HaloTag and Halo-CTD fusions bulk wide-field staining using JFX650 in live cell. Scale bar: 1.0 μm. **c**, Nucleoplasm/Nucleolus ratios for freely diffusing HaloTag and Halo-CTD fusions (n = 100 resamplings; mean value ± s.d.). **d**, Protein disorder affects hydrodynamic radius (R_h). **e**, Theoretical relationship between molecule weight and R_h for folded and unfolded peptides (Data from Fluidic Analytics). **f-g**, **f**, D_{free} and estimated R_h of the HaloTag and Halo-CTD fusions in nucleoplasm and nucleolus. Data fitted with Stokes-Einstein equation to calculate **g**, apparent viscosity (η) of yeast nucleoplasm (NPL) and nucleolus (NOL), respectively. K_B: Boltzmann's constant. T: Temperature in Kelvin; 295.15K (22°C) (n = 100 resamplings; mean value ± s.d.). **h**, $f_{180/0}$ plot for HaloTag and Halo-CTD fusions (n = 100 resamplings; mean value ± s.d.). Source numerical data are available in source data.

Supplementary Material

Refer to Web version on PubMed Central for supplementary material.

Acknowledgments

We thank Scarlet Cho and Gan Ling for assistance in image processing; Luke Lavis for providing Janelia Fluor dyes; Kelly Xie for IUPRED3 data mining; Xiaona Tang and Sheng Liu for computational assistance; Nathan Jones, Vincent Schoonderwoert and Ciprian Almonte for microscopy technical support; Karen Yuen and Gaku Mizuguchi for plasmids and yeast strains; Craig Kaplan and Joanna Yao for valuable information on strain-sensitivity to MPA; Anders Hansen, Andrea Musacchio, Charmaine Wong, Ibrahim Cissé and Jee Min Kim for helpful discussions; and members of the Wu laboratory for comments. This study was supported by National Institute of Health grant GM132290 and R35GM149291 (C.W.) and the Croucher Foundation (Y.H.L.).

Data availability

Raw single-molecule trajectory coordinates are accessible at Zenodo (https://zenodo.org/records/10570246). Source data have been provided in Source Data. All other data supporting the findings of this study are available from the corresponding author on reasonable request.

References

1. Cramer P, Bushnell DA & Kornberg RD Structural basis of transcription: RNA polymerase II at 2.8 angstrom resolution. Science 292, 1863–1876, doi:10.1126/science.1059493 (2001). [PubMed: 11313498]
2. Corden JL RNA polymerase II C-terminal domain: Tethering transcription to transcript and template. Chem Rev 113, 8423–8455, doi:10.1021/cr400158h (2013). [PubMed: 24040939]
3. Eick D & Geyer M The RNA polymerase II carboxy-terminal domain (CTD) code. Chem Rev 113, 8456–8490, doi:10.1021/cr400071f (2013). [PubMed: 23952966]
4. Harlen KM & Churchman LS The code and beyond: transcription regulation by the RNA polymerase II carboxy-terminal domain. Nat Rev Mol Cell Biol 18, 263–273, doi:10.1038/nrm.2017.10 (2017). [PubMed: 28248323]
5. Buratowski S Progression through the RNA polymerase II CTD cycle. Mol Cell 36, 541–546, doi:10.1016/j.molcel.2009.10.019 (2009). [PubMed: 19941815]
6. Thompson CM, Koleske AJ, Chao DM & Young RA A multisubunit complex associated with the RNA polymerase II CTD and TATA-binding protein in yeast. Cell 73, 1361–1375, doi:10.1016/0092-8674(93)90362-t (1993). [PubMed: 8324825]
7. West ML & Corden JL Construction and analysis of yeast RNA polymerase II CTD deletion and substitution mutations. Genetics 140, 1223–1233, doi:10.1093/genetics/140.4.1223 (1995). [PubMed: 7498765]
8. Hsin JP, Sheth A & Manley JL RNAP II CTD phosphorylated on threonine-4 is required for histone mRNA 3' end processing. Science 334, 683–686, doi:10.1126/science.1206034 (2011). [PubMed: 22053051]
9. Bartolomei MS, Halden NF, Cullen CR & Corden JL Genetic analysis of the repetitive carboxyl-terminal domain of the largest subunit of mouse RNA polymerase II. Mol Cell Biol 8, 330–339, doi:10.1128/mcb.8.1.330-339.1988 (1988). [PubMed: 3275873]
10. Litingtung Y et al. Growth retardation and neonatal lethality in mice with a homozygous deletion in the C-terminal domain of RNA polymerase II. Mol Gen Genet 261, 100–105, doi:10.1007/s004380050946 (1999). [PubMed: 10071215]
11. Babokhov M, Mosaheb MM, Baker RW & Fuchs SM Repeat-Specific Functions for the C-Terminal Domain of RNA Polymerase II in Budding Yeast. G3 (Bethesda) 8, 1593–1601, doi:10.1534/g3.118.200086 (2018). [PubMed: 29523636]

12. Meisels E, Gileadi O & Corden JL Partial truncation of the yeast RNA polymerase II carboxyl-terminal domain preferentially reduces expression of glycolytic genes. J Biol Chem 270, 31255–31261, doi:10.1074/jbc.270.52.31255 (1995). [PubMed: 8537392]
13. Quintero-Cadena P, Lenstra TL & Sternberg PW RNA Pol II Length and Disorder Enable Cooperative Scaling of Transcriptional Bursting. Mol Cell 79, 207–220 e208, doi:10.1016/j.molcel.2020.05.030 (2020). [PubMed: 32544389]
14. Sawicka A et al. Transcription activation depends on the length of the RNA polymerase II C-terminal domain. EMBO J 40, e107015, doi:10.15252/embj.2020107015 (2021). [PubMed: 33555055]
15. Allison LA & Ingles CJ Mutations in RNA polymerase II enhance or suppress mutations in GAL4. Proc Natl Acad Sci U S A 86, 2794–2798, doi:10.1073/pnas.86.8.2794 (1989). [PubMed: 2495535]
16. Scafe C et al. RNA polymerase II C-terminal repeat influences response to transcriptional enhancer signals. Nature 347, 491–494, doi:10.1038/347491a0 (1990). [PubMed: 2215664]
17. Gerber HP et al. RNA polymerase II C-terminal domain required for enhancer-driven transcription. Nature 374, 660–662, doi:10.1038/374660a0 (1995). [PubMed: 7715709]
18. Chapman RD, Heidemann M, Hintermair C & Eick D Molecular evolution of the RNA polymerase II CTD. Trends Genet 24, 289–296, doi:10.1016/j.tig.2008.03.010 (2008). [PubMed: 18472177]
19. Yang C & Stiller JW Evolutionary diversity and taxon-specific modifications of the RNA polymerase II C-terminal domain. Proc Natl Acad Sci U S A 111, 5920–5925, doi:10.1073/pnas.1323616111 (2014). [PubMed: 24711388]
20. Boehning M et al. RNA polymerase II clustering through carboxy-terminal domain phase separation. Nat Struct Mol Biol 25, 833–840, doi:10.1038/s41594-018-0112-y (2018). [PubMed: 30127355]
21. Lu H et al. Phase-separation mechanism for C-terminal hyperphosphorylation of RNA polymerase II. Nature 558, 318–323, doi:10.1038/s41586-018-0174-3 (2018). [PubMed: 29849146]
22. Guo YE et al. Pol II phosphorylation regulates a switch between transcriptional and splicing condensates. Nature 572, 543–548, doi:10.1038/s41586-019-1464-0 (2019). [PubMed: 31391587]
23. Cho WK et al. RNA Polymerase II cluster dynamics predict mRNA output in living cells. Elife 5, doi:10.7554/eLife.13617 (2016).
24. Cisse II et al. Real-time dynamics of RNA polymerase II clustering in live human cells. Science 341, 664–667, doi:10.1126/science.1239053 (2013). [PubMed: 23828889]
25. Cho WK et al. Mediator and RNA polymerase II clusters associate in transcription-dependent condensates. Science 361, 412–415, doi:10.1126/science.aar4199 (2018). [PubMed: 29930094]
26. Boija A et al. Transcription Factors Activate Genes through the Phase-Separation Capacity of Their Activation Domains. Cell 175, 1842–1855 e1816, doi:10.1016/j.cell.2018.10.042 (2018). [PubMed: 30449618]
27. Wei MT et al. Nucleated transcriptional condensates amplify gene expression. Nat Cell Biol 22, 1187–1196, doi:10.1038/s41556-020-00578-6 (2020). [PubMed: 32929202]
28. McSwiggen DT, Mir M, Darzacq X & Tjian R Evaluating phase separation in live cells: diagnosis, caveats, and functional consequences. Genes Dev 33, 1619–1634, doi:10.1101/gad.331520.119 (2019). [PubMed: 31594803]
29. Musacchio A On the role of phase separation in the biogenesis of membraneless compartments. EMBO J 41, e109952, doi:10.15252/embj.2021109952 (2022). [PubMed: 35107832]
30. Chong S et al. Imaging dynamic and selective low-complexity domain interactions that control gene transcription. Science 361, doi:10.1126/science.aar2555 (2018).
31. Palacio M & Taatjes DJ Merging Established Mechanisms with New Insights: Condensates, Hubs, and the Regulation of RNA Polymerase II Transcription. J Mol Biol 434, 167216, doi:10.1016/j.jmb.2021.167216 (2022). [PubMed: 34474085]
32. Tjong H, Gong K, Chen L & Alber F Physical tethering and volume exclusion determine higher-order genome organization in budding yeast. Genome Res 22, 1295–1305, doi:10.1101/gr.129437.111 (2012). [PubMed: 22619363]

33. Gasser SM, Hediger F, Taddei A, Neumann FR & Gartenberg MR The function of telomere clustering in yeast: the circe effect. Cold Spring Harb Symp Quant Biol 69, 327–337, doi:10.1101/sqb.2004.69.327 (2004). [PubMed: 16117665]
34. Rosa A & Everaers R Structure and dynamics of interphase chromosomes. PLoS Comput Biol 4, e1000153, doi:10.1371/journal.pcbi.1000153 (2008). [PubMed: 18725929]
35. Zimmer C & Fabre E Principles of chromosomal organization: lessons from yeast. J Cell Biol 192, 723–733, doi:10.1083/jcb.201010058 (2011). [PubMed: 21383075]
36. Berger AB et al. High-resolution statistical mapping reveals gene territories in live yeast. Nat Methods 5, 1031–1037, doi:10.1038/nmeth.1266 (2008). [PubMed: 18978785]
37. Duan Z et al. A three-dimensional model of the yeast genome. Nature 465, 363–367, doi:10.1038/nature08973 (2010). [PubMed: 20436457]
38. Miura F et al. Absolute quantification of the budding yeast transcriptome by means of competitive PCR between genomic and complementary DNAs. BMC Genomics 9, 574, doi:10.1186/1471-2164-9-574 (2008). [PubMed: 19040753]
39. Gong K, Tjong H, Zhou XJ & Alber F Comparative 3D genome structure analysis of the fission and the budding yeast. PLoS One 10, e0119672, doi:10.1371/journal.pone.0119672 (2015). [PubMed: 25799503]
40. Tokuda N & Sasai M Heterogeneous Spatial Distribution of Transcriptional Activity in Budding Yeast Nuclei. Biophys J 112, 491–504, doi:10.1016/j.bpj.2016.11.3201 (2017). [PubMed: 28040197]
41. Huisinga KL & Pugh BF A genome-wide housekeeping role for TFIID and a highly regulated stress-related role for SAGA in Saccharomyces cerevisiae. Mol Cell 13, 573–585, doi:10.1016/s1097-2765(04)00087-5 (2004). [PubMed: 14992726]
42. Erickson HP Size and shape of protein molecules at the nanometer level determined by sedimentation, gel filtration, and electron microscopy. Biol Proced Online 11, 32–51, doi:10.1007/s12575-009-9008-x (2009). [PubMed: 19495910]
43. Portz B et al. Structural heterogeneity in the intrinsically disordered RNA polymerase II C-terminal domain. Nat Commun 8, 15231, doi:10.1038/ncomms15231 (2017). [PubMed: 28497792]
44. Hansen AS, Amitai A, Cattoglio C, Tjian R & Darzacq X Guided nuclear exploration increases CTCF target search efficiency. Nat Chem Biol 16, 257–266, doi:10.1038/s41589-019-0422-3 (2020). [PubMed: 31792445]
45. Gartenberg MR, Neumann FR, Laroche T, Blaszczyk M & Gasser SM Sir-mediated repression can occur independently of chromosomal and subnuclear contexts. Cell 119, 955–967, doi:10.1016/j.cell.2004.11.008 (2004). [PubMed: 15620354]
46. Mazzocca M et al. Chromatin organization drives the search mechanism of nuclear factors. Nat Commun 14, 6433, doi:10.1038/s41467-023-42133-5 (2023). [PubMed: 37833263]
47. Hansen AS, Pustova I, Cattoglio C, Tjian R & Darzacq X CTCF and cohesin regulate chromatin loop stability with distinct dynamics. Elife 6, doi:10.7554/eLife.25776 (2017).
48. Baek I, Friedman LJ, Gelles J & Buratowski S Single-molecule studies reveal branched pathways for activator-dependent assembly of RNA polymerase II pre-initiation complexes. Mol Cell 81, 3576–3588 e3576, doi:10.1016/j.molcel.2021.07.025 (2021). [PubMed: 34384542]
49. Schilbach S, Wang H, Dienemann C & Cramer P Yeast PIC-Mediator structure with RNA polymerase II C-terminal domain. Proc Natl Acad Sci U S A 120, e2220542120, doi:10.1073/pnas.2220542120 (2023). [PubMed: 37014863]
50. Yahia Y et al. RNA polymerase II CTD is dispensable for transcription and required for termination in human cells. EMBO Rep 24, e56150, doi:10.15252/embr.202256150 (2023). [PubMed: 37424514]
51. Warfield L et al. Transcription of Nearly All Yeast RNA Polymerase II-Transcribed Genes Is Dependent on Transcription Factor TFIID. Mol Cell 68, 118–129 e115, doi:10.1016/j.molcel.2017.08.014 (2017). [PubMed: 28918900]
52. Robinson PJ, Bushnell DA, Trnka MJ, Burlingame AL & Kornberg RD Structure of the mediator head module bound to the carboxy-terminal domain of RNA polymerase II. Proc Natl Acad Sci U S A 109, 17931–17935, doi:10.1073/pnas.1215241109 (2012). [PubMed: 23071300]

53. Wu C Heat shock transcription factors: structure and regulation. Annu Rev Cell Dev Biol 11, 441–469, doi:10.1146/annurev.cb.11.110195.002301 (1995). [PubMed: 8689565]

54. Jakobsen BK & Pelham HR Constitutive binding of yeast heat shock factor to DNA in vivo. Mol Cell Biol 8, 5040–5042, doi:10.1128/mcb.8.11.5040-5042.1988 (1988). [PubMed: 3062378]

55. Park HO & Craig EA Positive and negative regulation of basal expression of a yeast HSP70 gene. Mol Cell Biol 9, 2025–2033, doi:10.1128/mcb.9.5.2025-2033.1989 (1989). [PubMed: 2664467]

56. Sorger PK & Pelham HR Purification and characterization of a heat-shock element binding protein from yeast. EMBO J 6, 3035–3041, doi:10.1002/j.1460-2075.1987.tb02609.x (1987). [PubMed: 3319580]

57. Sorger PK & Pelham HR Yeast heat shock factor is an essential DNA-binding protein that exhibits temperature-dependent phosphorylation. Cell 54, 855–864, doi:10.1016/s0092-8674(88)91219-6 (1988). [PubMed: 3044613]

58. Sewitz SA et al. Heterogeneous chromatin mobility derived from chromatin states is a determinant of genome organisation in S. cerevisiae. bioRxiv, 106344, doi:10.1101/106344 (2017).

59. Hnisz D, Shrinivas K, Young RA, Chakraborty AK & Sharp PA A Phase Separation Model for Transcriptional Control. Cell 169, 13–23, doi:10.1016/j.cell.2017.02.007 (2017). [PubMed: 28340338]

60. Lyons H et al. Functional partitioning of transcriptional regulators by patterned charge blocks. Cell 186, 327–345 e328, doi:10.1016/j.cell.2022.12.013 (2023). [PubMed: 36603581]

61. Zhao ZW et al. Spatial organization of RNA polymerase II inside a mammalian cell nucleus revealed by reflected light-sheet superresolution microscopy. Proc Natl Acad Sci U S A 111, 681–686, doi:10.1073/pnas.1318496111 (2014). [PubMed: 24379392]

62. Lu F, Portz B & Gilmour DS The C-Terminal Domain of RNA Polymerase II Is a Multivalent Targeting Sequence that Supports Drosophila Development with Only Consensus Heptads. Mol Cell 73, 1232–1242 e1234, doi:10.1016/j.molcel.2019.01.008 (2019). [PubMed: 30765194]

63. Kovacs D et al. HSF1Base: A Comprehensive Database of HSF1 (Heat Shock Factor 1) Target Genes. Int J Mol Sci 20, doi:10.3390/ijms20225815 (2019).

64. Pincus D et al. Genetic and epigenetic determinants establish a continuum of Hsf1 occupancy and activity across the yeast genome. Mol Biol Cell 29, 3168–3182, doi:10.1091/mbc.E18-06-0353 (2018). [PubMed: 30332327]

Methods-only references

65. Therizols P, Duong T, Dujon B, Zimmer C & Fabre E Chromosome arm length and nuclear constraints determine the dynamic relationship of yeast subtelomeres. Proc Natl Acad Sci U S A 107, 2025–2030, doi:10.1073/pnas.0914187107 (2010). [PubMed: 20080699]

66. Taddei A & Gasser SM Structure and function in the budding yeast nucleus. Genetics 192, 107–129, doi:10.1534/genetics.112.140608 (2012). [PubMed: 22964839]

67. Tsai KL et al. A conserved Mediator-CDK8 kinase module association regulates Mediator-RNA polymerase II interaction. Nat Struct Mol Biol 20, 611–619, doi:10.1038/nsmb.2549 (2013). [PubMed: 23563140]

68. Knuesel MT, Meyer KD, Bernecky C & Taatjes DJ The human CDK8 subcomplex is a molecular switch that controls Mediator coactivator function. Genes Dev 23, 439–451, doi:10.1101/gad.1767009 (2009). [PubMed: 19240132]

69. Elmlund H et al. The cyclin-dependent kinase 8 module sterically blocks Mediator interactions with RNA polymerase II. Proc Natl Acad Sci U S A 103, 15788–15793, doi:10.1073/pnas.0607483103 (2006). [PubMed: 17043218]

70. Mazza D, Abernathy A, Golob N, Morisaki T & McNally JG A benchmark for chromatin binding measurements in live cells. Nucleic Acids Res 40, e119, doi:10.1093/nar/gks701 (2012). [PubMed: 22844090]

71. Zhao T et al. Ssl2/TFIIH function in transcription start site scanning by RNA polymerase II in Saccharomyces cerevisiae. Elife 10, doi:10.7554/eLife.71013 (2021).

72. Lenstra TL & Larson DR Single-Molecule mRNA Detection in Live Yeast. Curr Protoc Mol Biol 113, 14 24 11–14 24 15, doi:10.1002/0471142727.mb1424s113 (2016).

73. Nguyen VQ et al. Spatiotemporal coordination of transcription preinitiation complex assembly in live cells. Mol Cell 81, 3560–3575 e3566, doi:10.1016/j.molcel.2021.07.022 (2021). [PubMed: 34375585]
74. Zheng Q et al. Rational Design of Fluorogenic and Spontaneously Blinking Labels for Super-Resolution Imaging. ACS Cent Sci 5, 1602–1613, doi:10.1021/acscentsci.9b00676 (2019). [PubMed: 31572787]
75. Grimm JB et al. A general method to improve fluorophores for live-cell and single-molecule microscopy. Nat Methods 12, 244–250, 243 p following 250, doi:10.1038/nmeth.3256 (2015). [PubMed: 25599551]
76. Vallotton P et al. Diatrack particle tracking software: Review of applications and performance evaluation. Traffic 18, 840–852, doi:10.1111/tra.12530 (2017). [PubMed: 28945316]
77. Persson F, Linden M, Unoson C & Elf J Extracting intracellular diffusive states and transition rates from single-molecule tracking data. Nat Methods 10, 265–269, doi:10.1038/nmeth.2367 (2013). [PubMed: 23396281]
78. Kim JM et al. Single-molecule imaging of chromatin remodelers reveals role of ATPase in promoting fast kinetics of target search and dissociation from chromatin. Elife 10, doi:10.7554/eLife.69387 (2021).
79. Teves SS et al. A stable mode of bookmarking by TBP recruits RNA polymerase II to mitotic chromosomes. Elife 7, doi:10.7554/eLife.35621 (2018).
80. Medler S et al. Evidence for a complex of transcription factor IIB with poly(A) polymerase and cleavage factor 1 subunits required for gene looping. J Biol Chem 286, 33709–33718, doi:10.1074/jbc.M110.193870 (2011). [PubMed: 21835917]
81. Vink JNA, Brouns SJJ & Hohlbein J Extracting Transition Rates in Particle Tracking Using Analytical Diffusion Distribution Analysis. Biophys J 119, 1970–1983, doi:10.1016/j.bpj.2020.09.033 (2020). [PubMed: 33086040]
82. Park S et al. Dynamic interactions between the RNA chaperone Hfq, small regulatory RNAs, and mRNAs in live bacterial cells. Elife 10, doi:10.7554/eLife.64207 (2021).
83. Hansen AS et al. Robust model-based analysis of single-particle tracking experiments with Spot-On. Elife 7, doi:10.7554/eLife.33125 (2018).
84. Heckert A, Dahal L, Tjian R & Darzacq X Recovering mixtures of fast-diffusing states from short single-particle trajectories. Elife 11, doi:10.7554/eLife.70169 (2022).
85. Wagner T, Kroll A, Haramagatti CR, Lipinski HG & Wiemann M Classification and Segmentation of Nanoparticle Diffusion Trajectories in Cellular Micro Environments. PLoS One 12, e0170165, doi:10.1371/journal.pone.0170165 (2017). [PubMed: 28107406]
86. Pinholt HD, Bohr SS, Iversen JF, Boomsma W & Hatzakis NS Single-particle diffusional fingerprinting: A machine-learning framework for quantitative analysis of heterogeneous diffusion. Proc Natl Acad Sci U S A 118, doi:10.1073/pnas.2104624118 (2021).
87. Saxton MJ Lateral diffusion in an archipelago. Single-particle diffusion. Biophys J 64, 1766–1780, doi:10.1016/S0006-3495(93)81548-0 (1993). [PubMed: 8369407]
88. Koo PK & Mochrie SG Systems-level approach to uncovering diffusive states and their transitions from single-particle trajectories. Phys Rev E 94, 052412, doi:10.1103/PhysRevE.94.052412 (2016). [PubMed: 27967069]
89. Kapadia N, El-Hajj ZW & Reyes-Lamothe R Bound2Learn: a machine learning approach for classification of DNA-bound proteins from single-molecule tracking experiments. Nucleic Acids Res 49, e79, doi:10.1093/nar/gkab186 (2021). [PubMed: 33744965]
90. Luan J et al. Distinct properties and functions of CTCF revealed by a rapidly inducible degron system. Cell Rep 34, 108783, doi:10.1016/j.celrep.2021.108783 (2021). [PubMed: 33626344]
91. Chazeau A, Katrukha EA, Hoogenraad CC & Kapitein LC Studying neuronal microtubule organization and microtubule-associated proteins using single molecule localization microscopy. Methods Cell Biol 131, 127–149, doi:10.1016/bs.mcb.2015.06.017 (2016). [PubMed: 26794511]
92. Bohrer CH et al. A pairwise distance distribution correction (DDC) algorithm to eliminate blinking-caused artifacts in SMLM. Nat Methods 18, 669–677, doi:10.1038/s41592-021-01154-y (2021). [PubMed: 34059826]

93. Morawska M & Ulrich HD An expanded tool kit for the auxin-inducible degron system in budding yeast. Yeast 30, 341–351, doi:10.1002/yea.2967 (2013). [PubMed: 23836714]

94. Papagiannakis A, de Jonge JJ, Zhang Z & Heinemann M Quantitative characterization of the auxin-inducible degron: a guide for dynamic protein depletion in single yeast cells. Sci Rep 7, 4704, doi:10.1038/s41598-017-04791-6 (2017). [PubMed: 28680098]

95. Gesnel MC, Del Gatto-Konczak F & Breathnach R Combined use of MS2 and PP7 coat fusions shows that TIA-1 dominates hnRNP A1 for K-SAM exon splicing control. J Biomed Biotechnol 2009, 104853, doi:10.1155/2009/104853 (2009). [PubMed: 20130820]

96. Brouwer I, Kerklingh E, van Leeuwen F & Lenstra TL Dynamic epistasis analysis reveals how chromatin remodeling regulates transcriptional bursting. Nat Struct Mol Biol, doi:10.1038/s41594-023-00981-1 (2023).

97. Li L, Waymack R, Gad M & Wunderlich Z Two promoters integrate multiple enhancer inputs to drive wild-type knirps expression in the Drosophila melanogaster embryo. Genetics 219, doi:10.1093/genetics/iyab154 (2021).

98. Zhang T et al. An improved method for whole protein extraction from yeast Saccharomyces cerevisiae. Yeast 28, 795–798, doi:10.1002/yea.1905 (2011). [PubMed: 21972073]

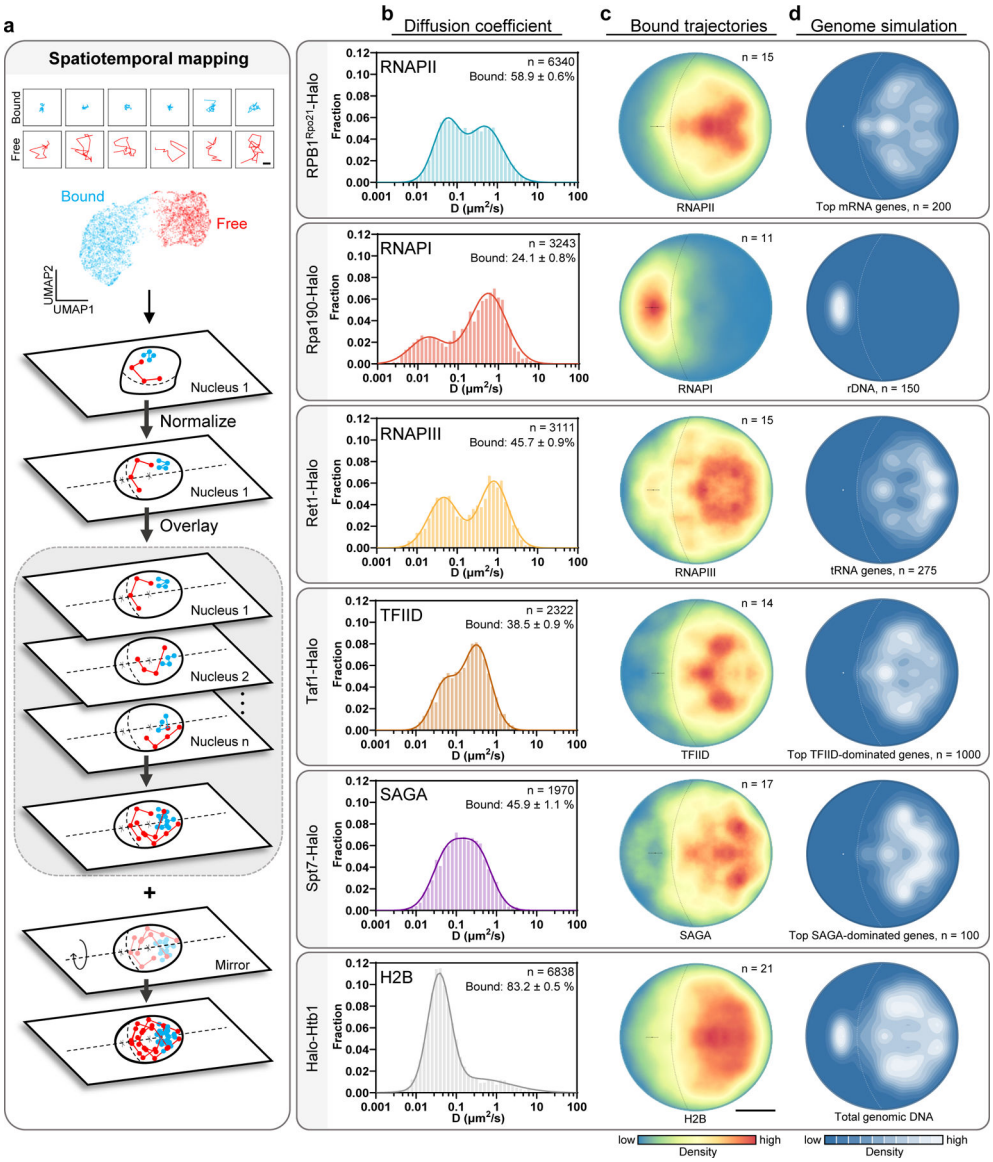

Figure 1. Spatiotemporal mapping of transcription machinery in living yeast nucleus.

a, Spatiotemporal mapping workflow: bound and free trajectories (Scale bar: 0.2 μm) classified by multi-parameter analysis, and single-molecule localization and nuclear radius normalized to a circular model of 1 μm radius. Localizations overlaid from at least 10 nuclei that display minimal drift during image acquisition. Visualization of the spatiotemporal map on a single plane facilitated by mirroring around the central axis[36]. **b**, Diffusion coefficient histograms for RNAPII, RNAPI, RNAPIII, TFIID, SAGA and H2B. Representative HaloTag fusions shown (n: number of trajectories; mean value ± s.d.). **c**, Detection map of chromatin-bound trajectories. Scale bar: 0.5 μm (Error bar: centroid of nucleolus ± s.d.; n: number of nuclei). **d**, Simulation of the spatial distribution of gene classes in yeast nucleus (n: number of genes). Source numerical data are available in source data.

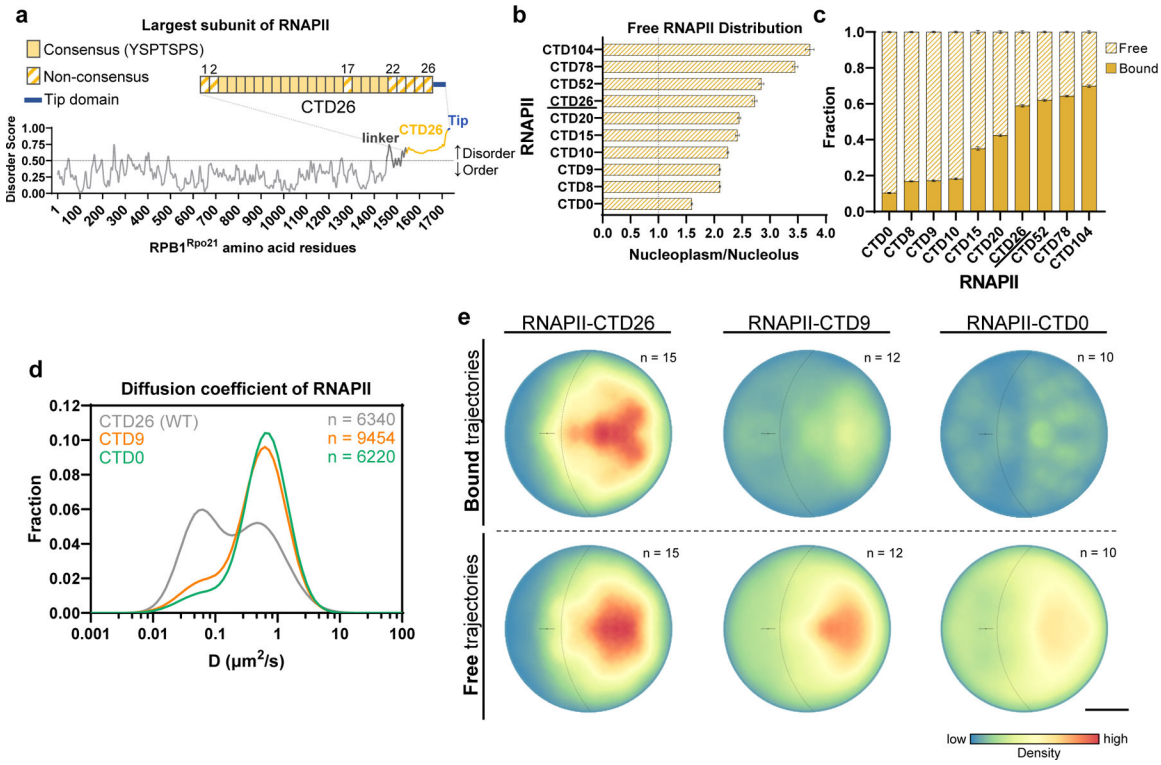

Figure 2. CTD governs spatiotemporal dynamics of RNAPII.

a, Disordered C-terminal domain of RPB1^{Rpo21} consisting of 26 heptad repeats with consensus sequence YSPTSPS. IUPRED3 scores above 0.5 considered disordered. **b-e**, Spatiotemporal dynamics of RNAPII and CTD mutants characterized by **b**, ratio of freely diffusing molecules between the nucleoplasm and nucleolus (n = 100 resamplings; mean value ± s.d.), **c**, fraction of free and bound (n = 100 resamplings; mean value ± s.d.), **d**, two-component Gaussian fit of diffusion coefficient histograms, and **e**, spatiotemporal mapping for bound and free trajectories. Scale bar: 0.5 μm (Error bar: centroid of nucleolus ± s.d.; n: number of nuclei). Top left panel is reuse of Fig. 1c top panel. Source numerical data are available in source data.

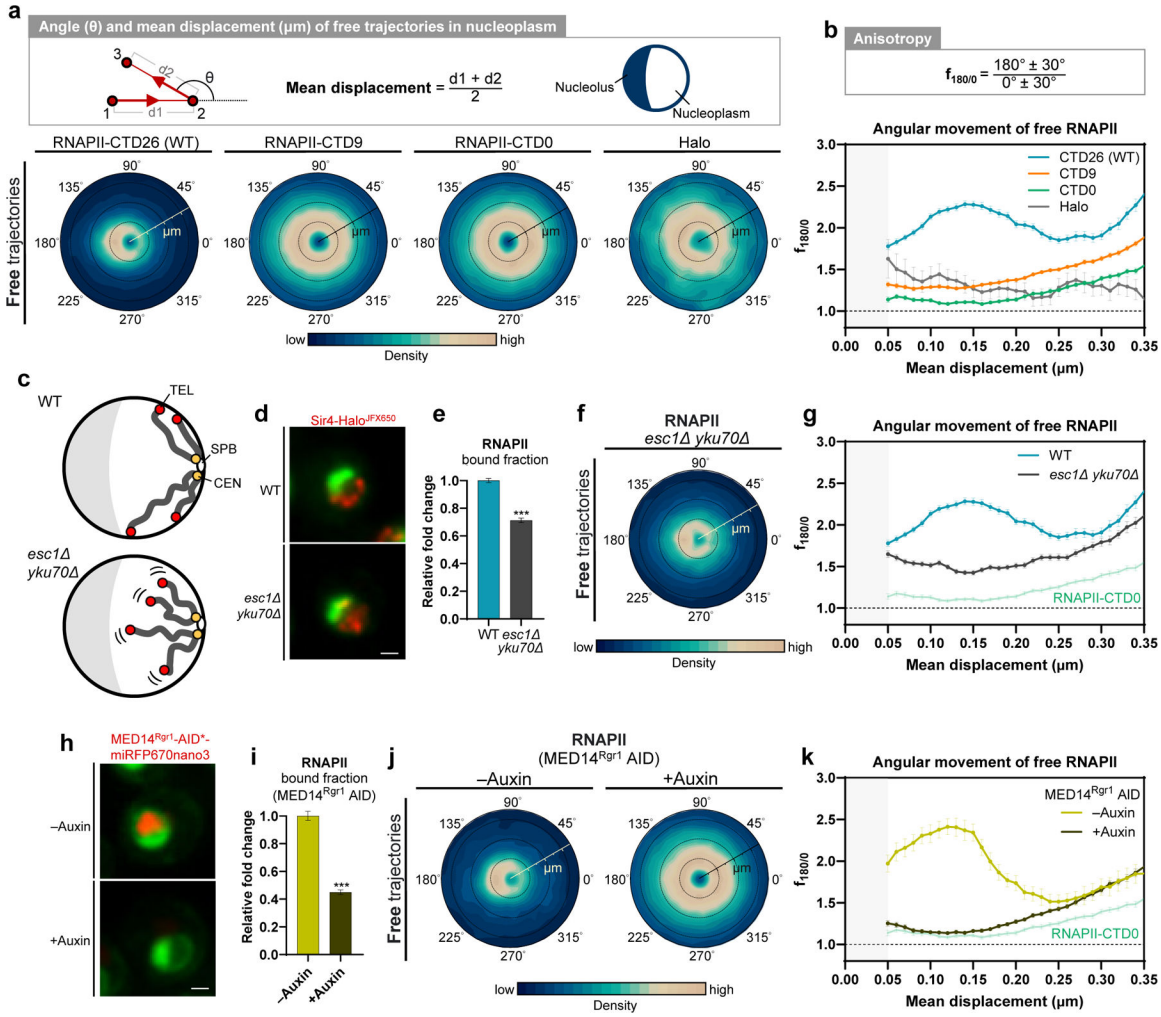

Figure 3. The interplay of CTD, chromatin organization and Mediator shapes RNAPII anisotropic diffusion.

a, Angle (angular axis) and mean displacement (radial axis; unit: μm; major tick interval = 0.1 μm) polar plots of RNAPII, CTD mutants and HaloTag (NLSx2-Halo). **b**, Anisotropic diffusion of freely diffusing of RNAPII, CTD mutants and HaloTag in nucleoplasm measured by $f_{180/0}$ (n = 100 resamplings; mean value ± s.d.). **c**, Impaired telomere (TEL) attachment in *esc1Δ yku70Δ* strain. **d**, Fluorescence signal of Sir4-Halo^{JFX650} (red) in WT and *esc1Δ yku70Δ*. Nucleolar and ER markers in green. Scale bar: 1.0 μm (Supplementary Video 4). **e**, Relative bound fraction of RNAPII in WT and *esc1Δ yku70Δ* strains (n = 100 resamplings; mean value ± s.d.; two-tailed unpaired t-test, *** $P = 0.000287$). **f**, Angle and displacement polar plots of RNAPII in *esc1Δ yku70Δ* strain. **g**, $f_{180/0}$ of RNAPII in WT and *esc1Δ yku70Δ* strains (n = 100 resamplings; mean value ± s.d.). **h**, Fluorescence signal of MED14^{Rgr1}-AID*-miRFP670nano3 (red) before and after Mediator degradation by auxin treatment. Nucleolar and ER markers in green. Scale bar: 1.0 μm. **i**, Relative bound fraction of RNAPII after Mediator degradation (n = 100 resamplings; mean value ± s.d.; two-tailed unpaired t-test, *** $P = 0.000014$). **j**, Angle and displacement polar plots of RNAPII before

and after Mediator degradation. **k**, $f_{180/0}$ of RNAPII before and after Mediator degradation (n = 100 resamplings; mean value ± s.d.). Source numerical data are available in source data.

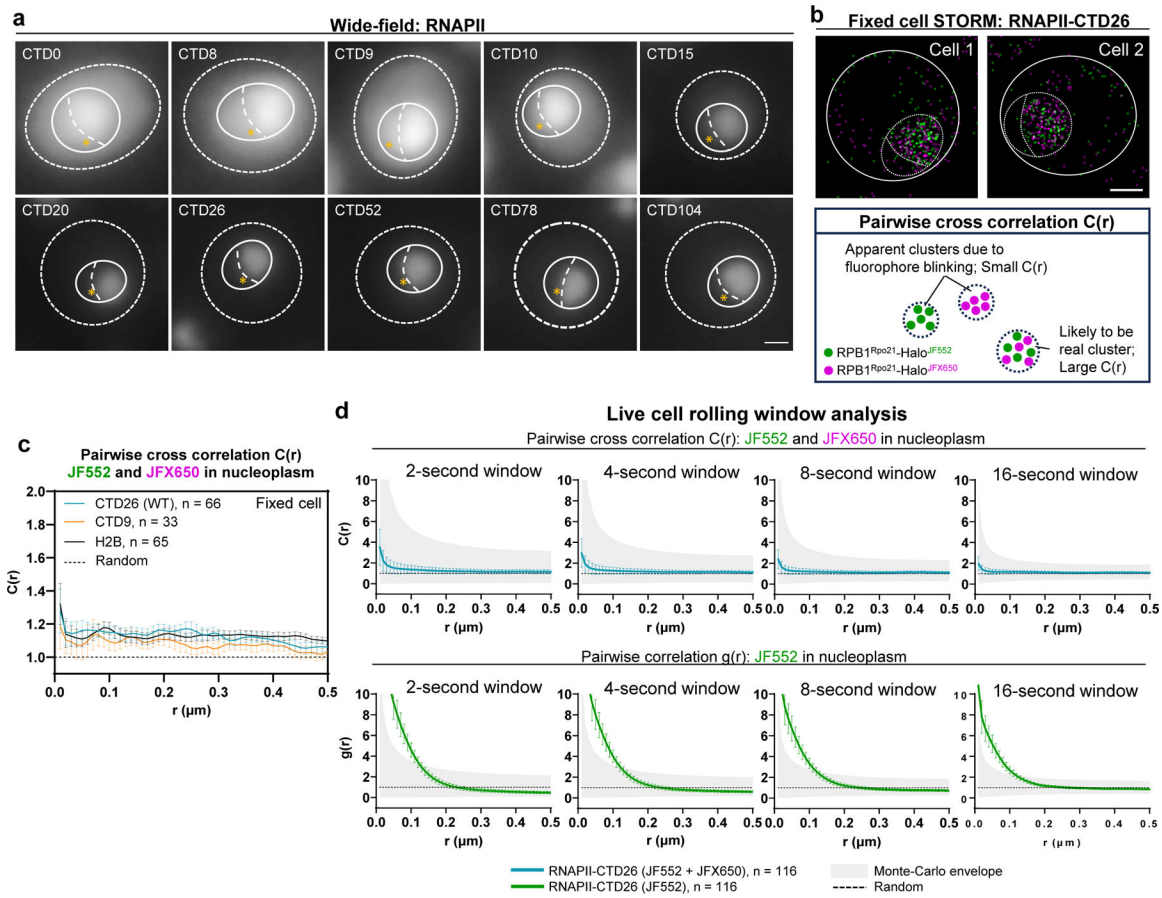

Figure 4. No substantial RNAPII clustering in yeast nucleoplasm.

a, Bulk wide-field staining of RPB1^{Rpo21}-Halo with JFX650 in live cells. Nucleolus indicated by asterisk. Scale bar: 1.0 μm. **b**, RPB1^{Rpo21}-Halo fixed-cell STORM images using JF552 and JFX650. Scale bar: 1.0 μm (top). RNAPII clustering analyzed by pairwise cross-correlation C(r) (bottom). **c**, C(r) of RNAPII-CTD26, RNAPII-CTD9 and H2B in nucleoplasm (n: number of nuclei; mean value ± s.d.). **d**, RPB1^{Rpo21}-Halo rolling window analysis for live cell two-color STORM (n: number of nuclei; mean value ± s.d.). Source numerical data are available in source data.

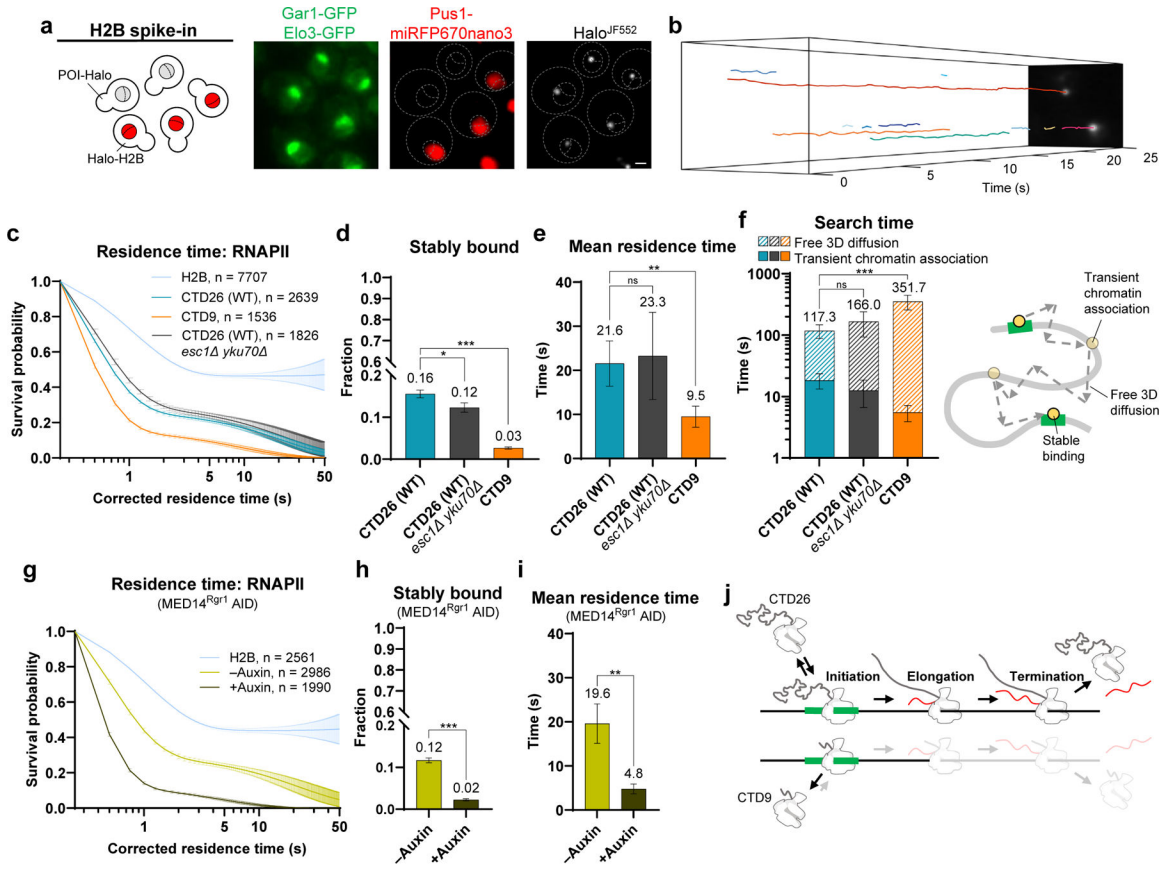

Figure 5. CTD facilitates RNAPII target-search kinetics.

a, Halo-H2B cell spike-in for residence time correction with Pus1-miRFP670nano3 nuclear marker. Scale bar: 1.0 μm. **b**, Kymograph of slow tracking trajectories of RNAPII (RPB1^{Rpo21}-Halo) (Supplementary Video 5). **c**, Survival probability of H2B-corrected residence times for bound RNAPII in CTD26 (WT), CTD9 and *esc1Δ yku70Δ* strains (n: number of trajectories; mean value ± s.d.). **d**-**f**, **d**, Stably bound fractions (n = 10,000 resamplings; mean value ± s.d.; two-tailed unpaired t-test, * P = 0.010109, *** P = 0.0000000267), **e**, mean residence times (n = 10,000 resamplings; mean value ± s.d.; two-tailed unpaired t-test, ns P = 0.762041, ** P = 0.003575), and **f**, search times (left) of RNAPII in CTD26 (WT), CTD9 and *esc1Δ yku70Δ* strains (n = 10,000 resamplings; mean value ± s.d.; two-tailed unpaired t-test, ns P = 0.220382, ** P = 0.001160). **f**, Simplified mode of target search in the nucleus (right). **g**, Survival probability of H2B-corrected residence times of RNAPII before and after Mediator degradation (MED14^{Rgr1} AID) (n: number of trajectories; mean value ± s.d.). **h**-**i**, **h**, Stably bound fractions (n = 10,000 resamplings; mean value ± s.d.; two-tailed unpaired t-test, *** P = 0.000013) and **i**, mean residence times of RNAPII before and after Mediator degradation (n = 10,000 resamplings; mean value ± s.d.; two-tailed unpaired t-test, ** P = 0.005117). **j**, Model of reduction of RNAPII residence time in CTD9 mutant. Source numerical data are available in source data.

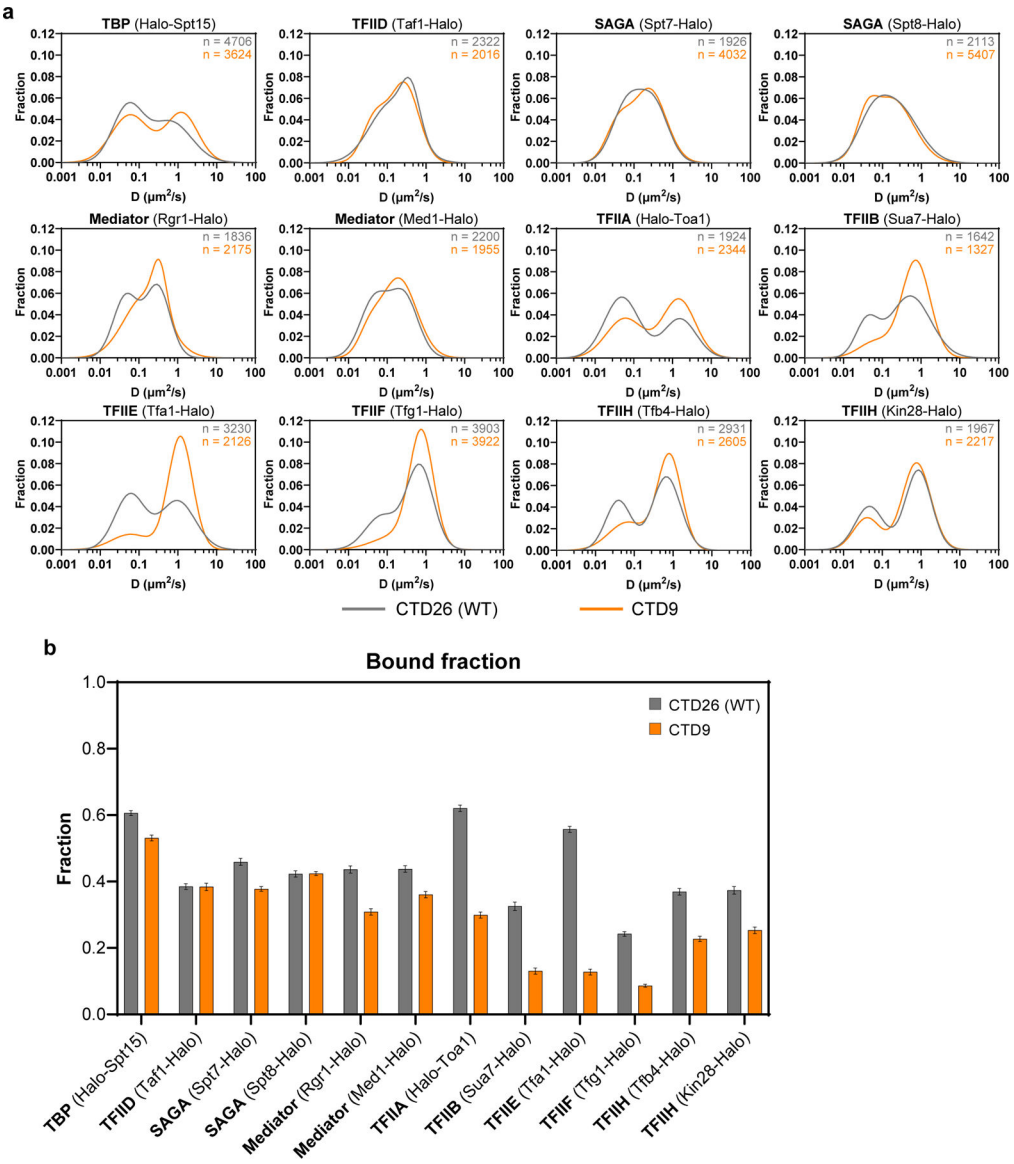

Figure 6. CTD truncation impairs PIC formation.

a, Diffusion histogram for TBP (Halo-Spt15), TFIID (Taf1-Halo), SAGA (Spt7-Halo and Spt8-Halo), Mediator (Rgr1-Halo and Med1-Halo), TFIIA (Halo-Toa1), TFIIB (Sua7-Halo), TFIIE (Tfa1-Halo), TFIIF (Tfg1-Halo) and TFIIH (Tfb4-Halo and Kin28-Halo) in WT and CTD9 strains (n: number of trajectories). **b**, Fraction free and bound in WT and CTD9 strains (n = 100 resamplings; mean value ± s.d.). Source numerical data are available in source data.

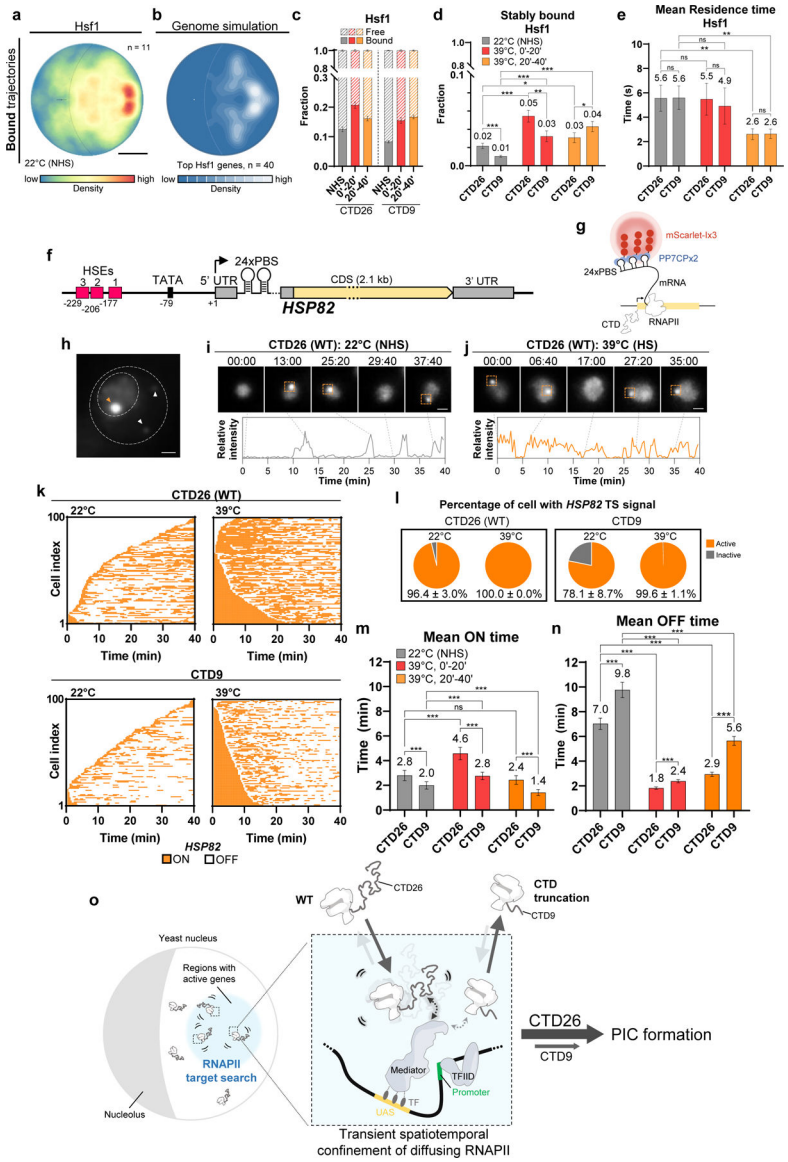

Figure 7. CTD length controls burst size and frequency of *HSP82* gene transcription.

a, Spatiotemporal map of bound Hsf1-Halo trajectories. Scale bar: 0.5 μm. **b**, Simulation of top Hsf1 target genes (HSF1Base[63]; n: number of genes). **c-e**, **c**, Fraction free and bound (n = 100 resamplings; mean value ± s.d.), **d**, stably bound fractions (n = 10,000 resamplings; mean value ± s.d.; two-tailed unpaired t-test, * $P \leq 0.05$, ** $P \leq 0.01$ and *** $P \leq 0.001$. Comparison between CTD26 and CTD9: $P = 0.000435$ for NHS, $P = 0.002398$ for 39°C, 0'−20', $P = 0.019571$ for 39°C, 20'−40'. Comparison between NHS and HS in CTD26: $P = 0.000095$ for 39°C, 0'−20', $P = 0.023496$ for 39°C, 20'−40'. Comparison between NHS and HS in CTD9: $P = 0.000371$ for 39°C, 0'−20', $P = 0.000027$ for 39°C, 20'−40') and **e**, mean residence times (n = 10,000 resamplings; mean value ± s.d.; two-tailed unpaired t-test, ** $P \leq 0.01$ and ns $P > 0.05$. Comparison between CTD26 and CTD9: $P = 0.957469$ for NHS, $P = 0.590303$ for 39°C, 0'−20', $P = 0.925673$ for 39°C, 20'−40'. Comparison between NHS and HS in CTD26: $P = 0.926090$ for 39°C, 0'−20', $P = 0.002251$ for 39°C,

20’−40’. Comparison between NHS and HS in CTD9: $P = 0.470398$ for 39°C, 0’−20’, $P = 0.001285$ for 39°C, 20’−40’) of Hsf1-Halo on heat shock (HS). CTD9 mutant shows similar upregulation of Hsf1 binding during acute heat shock (HS) compared to WT, but with slightly lower basal levels. Unlike WT, the CTD9 mutant maintains Hsf1 binding at the induced level during the prolonged response. The residence time of Hsf1 is comparable between WT and CTD9 under normal heat shock (NHS) and HS conditions. Overall, the dynamics of Hsf1 exhibit minimal change in CTD9 mutant. **f**, *HSP82* gene contains three characterized heat shock elements (HSEs) for Hsf1 binding[64]. 24x PP7 binding site (PBS) inserted within the 5’ UTR of *HSP82* gene. **g**, Nascent *HSP82* mRNA visualized by PP7CPx2-mScarlet-Ix3 binding. **h**, Nascent mRNAs on *HSP82* transcription site (TS) as a bright spot in the nucleus (orange arrow). Cytoplasmic *HSP82* mRNAs indicated by white arrows. Scale bar: 1.0 μm. **i-j**, Maximum z-projected time-lapse images of PP7-*HSP82* cells. Scale bar: 1.0 μm (top). Trace of relative fluorescence intensity of the transcription site (bottom). **k**, Binarized rastergrams of the PP7 signal at the *HSP82* TS of 100 cells, ordered by time of first detection. **l**, % cells with *HSP82* TS signal. **m-n**, **m**, Mean ON time (n = 10,000 resamplings; mean value ± s.d.; two-tailed unpaired t-test, *** $P \leq 0.001$ and ns $P > 0.05$. Comparison between CTD26 and CTD9: $P = 0.000202$ for NHS, $P = 0.000002$ for 39°C, 0’−20’, $P = 0.000041$ for 39°C, 20’−40’. Comparison between NHS and HS in CTD26: $P = 0.000608$ for 39°C, 0’−20’, $P = 0.198591$ for 39°C, 20’−40’. Comparison between NHS and HS in CTD9: $P = 0.000003$ for 39°C, 0’−20’, $P = 0.000049$ for 39°C, 20’−40’) and **n**, mean OFF time of *HSP82* transcription (n = 10,000 resamplings; mean value ± s.d.; two-tailed unpaired t-test, *** $P \leq 0.001$. Comparison between CTD26 and CTD9: $P = 0.00000008$ for NHS, $P = 0.000003$ for 39°C, 0’−20’, $P = 0.000000007$ for 39°C, 20’−40’. Comparison between NHS and HS in CTD26: $P = 0.0000001$ for 39°C, 0’−20’, $P = 0.0000007$ for 39°C, 20’−40’. Comparison between NHS and HS in CTD9: $P < 0.\ 000000001$ for 39°C, 0’−20’, $P < 0.\ 000000001$ for 39°C, 20’−40’). **o**, CTD directs subnuclear confinement and chromatin binding of RNAPII for efficient PIC assembly and transcription bursting. In the yeast nucleus, physical constraints such as telomere tethering of yeast chromosomes create subnuclear regions enriched with active genes (left blue circle). Within these regions, the diffusion of RNAPII is transiently confined (double parentheses), potentially through weak and long-range interaction (dashed arrows) between the CTD and the Mediator near an active promoter (middle square), leading to localized oversampling and enhanced target search efficiency. Such subnuclear confinement of freely diffusing RNAPII promotes the probability of intermolecular interactions and specific association rates for the formation of the multi-component PIC, and facilitates multiple rounds of RNAPII binding and activation for a transcription burst. TF: Transcription factor; UAS: Upstream activating sequence. Source numerical data are available in source data.